Pt(II)-bis(quinolinyl) complexes for photocatalytic hydrogen production

Rahat Gupta,[a] Olivier Schott,[b] Arindam Saha,[b,‡] Shriya,[a,‡] Garry S. Hanan[b] and Amlan K. Pal*[,a]

[a]Department of Chemistry, Indian Institute of Technology Jammu, Jagti Campus, Nagrota Bypass Road, Jammu & Kashmir, 181221, India
[b]Département de Chimie, Université de Montréal, Montréal, Québec H3C 3J7, Canada

‡Contributed equally

Supporting Information

Table of Contents

Materials, methods and instrumentation……....S2-S6
Synthetic schemes…….....S6-S9
Fig S1-S3: NMR data….....S9-S10
Fig S4-S6: XPS data……...S11-S13
Table S1: XPS data of **R1**, **1** and **R2**…….S13
Fig S7-S9: IR spectroscopic studies……...S14-S16
Fig S10-S13: PXRD data……....S16-S19
Table S2: Cell parameters form PXRD……..S19
Fig S14 Cyclic and squarewave voltammograms of **R1**, **1** and **R2**….....S19
Table S3 Electrochemical data of **R1**, **1** and **R2**…….....S19
Fig S15 Singlet DFT Calculation of **R1**, **1** and **R2**…….S20
Fig S16: Overlay of Experimental with predicted TD-DFT UV-visible transitions……...S20
Table S4 UV-visible absorption data of **R1**, **1** and **R2**…….S20
Table S5-S7: Selected TD-DFT predicted transitions **R1**, **1** and **R2**……..S21-S22
Fig S17. Chemical stability of Complexes……S22
Table S8: Photophysical data of **R1**, **1** and **R2,** respectively…….....S22
Fig S18: Emission spectra of LEDs used for H_2 production.....S23
Table S9: Absolute quantum yields for H_2 production…….S23
Fig S19: Stern-Volmer plot of $[Ru(bpy)_3]^{2+}$ with TEA…….....S23
Fig S20: Stern-Volmer plot of $[Ru(bpy)_3]^{2+}$ with **R1**…….....S24
Fig S21: Stern-Volmer plot of $[Ru(bpy)_3]^{2+}$ with **1**…….....S24
Fig S22: Stern-Volmer plot of $[Ru(bpy)_3]^{2+}$ with **R2**…….....S24
Fig S23-S24: Photoelectric properties of complexes……S25-S26
Fig S25-S27: Structural Stability of **R1**, **1** and **R2**.....S26-S27
Fig S28: H_2 evolution data of **R1**, **1** and **R2** without catalyst and PS…….....S28
Fig S29: FESEM images of **R1**…….....S28
Fig S30: FESEM images of **1**…….....S29
Fig S31-S39: Standard deviation calculations in TON……...S29-S33
Table S10: Photophysical properties of the LEDs used for H_2 production……S33-S34
Table S11-S13: XYZ coordinates of DFT optimized structures.....S34-S37
References……..S37-S38

Materials, methods and instrumentation

^{1}H and ^{13}C NMR spectra were recorded with a 500 MHz JEOL spectrometer (500 and 126 MHz for ^{1}H and ^{13}C, respectively) in the deuterated solvents as mentioned in the experimental section. The following abbreviations have been used for multiplicity assignments: "s" for singlet, "d" for doublet, "t" for triplet, "m" for multiplet, and "br" for broad. Chemical shifts are reported in parts per million (ppm) relative to respective residual solvent protons and coupling constants (J) are reported in Hertz (Hz). Chromatography was performed on columns with an i.d. of 25−30 mm on silica gel (Silica gel, 100−200 μm). The progress of the reactions and the elution of the products were followed by TLC (silica gel on plastic sheets, 250 μm with indicator F-254). Compounds were visualized under UV light. High-resolution mass spectra were recorded by Xevo, G2-XS QT in ESI^{+} mode. The material's morphology was characterized by FESEM (JEOL 7900F Prime). Panalytical powder XRD system (Empyrean, Cu Kα, λ = 1.5406 Å) was used to determine the crystalline nature of the samples. XPS spectra were measured using a Thermo Fisher Scientific (Nexsa) instrument with an Al Kα X-ray source. The XPS peak positions were normalized via deconvoluting the narrow region spectra of the particular element. We have used Thermo scientific "Avantage" software for peak deconvolution and fitting using the "simplex" algorithm with the "Shirley" function for background correction.

Photophysical measurements

All photophysical measurements were carried out in deaerated acetonitrile at RT in septa-sealed quartz cells. UV−vis spectroscopy (UV) was completed at room temperature using a Cary 5000 UV−vis spectrophotometer. All samples were prepared in HPLC grade MeCN, with varying concentrations in the order of 10^{-5}−10^{-6} M. Molar absorptivity determination was verified by a linear least-squares fit of values obtained from at least four independent solutions at varying concentrations. For steady state luminescence spectra at 298 K and 77 K, measurements in HPLC grade solvents containing the samples were excited at 360 nm using Shimadzu corp. spectrofluorimeter RF 6000. Emission quantum yields were determined using the optical dilution method.[1] A stock solution with an absorbance of *ca.* 1.0 was prepared and then four dilutions were prepared to obtain solutions with absorbance of *ca.* 0.100, 0.075, 0.05 and 0.025, respectively. The Beer-Lambert law was found to be linear at the concentrations of the solutions. The steady-state emission spectra (λ_{exc} = 360 nm) were then measured after the solutions were degassed in the N_2 atmosphere. For each sample, linearity between absorption

and emission intensity was verified through linear regression analysis and additional measurements were acquired until the Pearson regression factor (R^2) for the linear fit of the data set surpassed 0.9. Individual relative quantum yield values were calculated for each solution and the values reported represent the slope value. The equation $\Phi_s = \Phi_r(A_r/A_s)(I_s/I_r)(n_s/n_r)^2$ was used to calculate the relative quantum yield of each of the samples, where Φ_r is the absolute quantum yield of the reference, *n* is the refractive index of the solvent, *A* is the absorbance at the excitation wavelength and *I* is the integrated area under the corrected emission curve. The subscripts s and r refer to the sample and reference, respectively. Acetonitrile solution of quinine sulphate in 0.5 M H_2SO_4 ($\Phi_r = 54.6\%$) was used as the external reference.[2] Thin film PLQY measurements were performed using an integrating sphere in a Hammamatsu C9920-02 system.[3] Samples were excited by a xenon lamp coupled to a monochromator, which enabled selectivity of the excitation wavelength, chosen here to be 330 nm. The output was then fed into the integrating sphere via a fiber, exciting the sample. PL was collected with a multimode fibre and detected with a back-thinned CCD. The thin film PLQY were then measured in N_2 filled sphere.

Electrochemical measurements

Cyclic voltammetry (CV) measurements were performed on an Electrochemical Analyzer with potentiostat/Galvanostat (model no. CH660E) at a sweep rate of 100 mV/s. Solutions for CV were prepared in MeCN and degassed by purging nitrogen through the solutions for about 6 min before scanning. For supporting electrolytes Tetra(*n*-butyl)ammoniumhexafluorophosphate ($TBAPF_6$; *ca.* 0.1 M in MeCN) was used. For working, counter and reference electrodes Glassy carbon, platinum, and silver electrodes, were used. As an internal reference, ferrocene/ferrocenium (Fc/Fc^+) redox couple was used corresponding to a saturated calomel electrode (0.38 V *vs* SCE) [4] and the redox potentials were calibrated to this.

Theoretical Calculations.

All calculations were performed with the Gaussian16 employing the DFT method, the Becke three-parameter hybrid functional,[5] and Lee-Yang-Parr's gradient-corrected correlation functional (B3LYP).[6] Singlet ground state geometry optimizations for **R1**, **1** and **R2** were carried out at the (R)B3LYP level in the gas phase, using their respective Chem-3D optimized structures. All elements except Pt(II) were assigned the 6-31G(d,f) basis set.[7] The double-ζ quality SBKJC-VDZ basis set[8] with an effective core potential was employed for the Pt(II) atom. Vertical electronic excitations based on (R)B3LYP

optimized geometries were computed for **R1**, **1** and **R2** using the TD-DFT formalism[9, 10] in dichloromethane. Vibrational frequency calculations were performed to ensure that the optimized geometries represent the local minima and there are only positive eigenvalues. The electronic distribution and localization of the singlet excited states were visualized using the electron density difference maps (ED-DMs).[11] Gausssum 2.2 was employed to visualize the absorption spectra (simulated with Gaussian distribution with a full-width at half maximum (fwhm) set to 3000 cm^{-1}) and to calculate the fractional contributions of various groups to each molecular orbital.[12] All calculated structures were visualized with ChemCraft[13] and analysed with Chemissian.[14]

Photocatalytic hydrogen production

Photocatalytic hydrogen production: Monitoring of hydrogen evolution is measured using a Perkin Elmer Clarus-580 gas chromatograph (GC) with a thermal conductivity detector, argon as carrier and eluant gas, a 7' HayeSep N 60/80 pre-column, a 9' molecular sieve 13x45/60 column, and a 2 mL injection loop. The photoreactions are prepared in glovebox with dried and distilled DMF. Three distinct solutions were prepared, 1) photosensitizers, 2) catalyst, and 3) sacrificial donor and acid source (HBF4 48% water) to obtain 5 mL of sample solutions in standard 20 mL headspace vials. The resulting molar concentration of photocatalytic components are: 0.1 mM for the photosensitizers of Pt or $[Ru(bpy)_3][PF6]_2$, 1 mM for $[Co(dmgH)_2PyCl]$ and 6 mM for dimethylglyoxime, 0.5 M for triethanolamine and 0.05 mM for HBF4. The vials are placed on LED panel in a thermostatic bath set at 20°C. They were sealed with a rubber septum pierced with two stainless steel tubes. The first tube carried an argon flow pre-bubbled in spectrograde solvent. The flow was set to 10 ml/min (adjusted with a manual flow controller (Porter, 1000) and referenced with a digital flowmeter (Perkin Elmer FlowMark). The second tube led the flow to the GC sample loop through a 2 mL overflow protection vial, then through an 8-port stream select valve (VICCI) and finally to GC sample loop. A microprocessor (Arduino Uno) coupled with a custom PC interface allowed for timed injections. For calibration of H_2 production rate at a specific argon flow, a syringe pump (New Era Pump) equipped with a gas-tight syringe (SGE) and a 26s-gauge needle (Hamilton) was used to bubble different rates of pure hydrogen gas into the sample, to a minimum of 0.5 µL/minute. This gave a linear fit for peak area for H_2 versus the flow rates of H_2. For calibration testing, stock cylinders of known concentration of H_2 in argon replaced the argon flow (inserted at the pre-bubbler, to keep the same vapor matrix). The measured results, independent of flow

rate (under same pressure) can be easily converted into a rate of hydrogen following the equations mentioned below:

Quantification of H_2 by gas chromatography

A microprocessor (Arduino Uno) coupled with a custom PC interface controls the intervals (defined times) at which gas injections are taken from the reaction vial into the GC sample loop. A calibration curve, to establish the relationship (equation 1) between the integration of the H_2 and CO signal in the TCD trace (y) and the concentration of H_2 in the gas sample (x), is determined by flowing different, accurately known, concentrations of standard H_2 (balance of mixture is argon) into the sample loop and integrating the observed area under the H_2 peak in the TCD trace.

$$y = ax + b \qquad \text{eq (1)}$$

x = concentration of H_2, in $\mu L L^{-1}$ (known for calibration, but to be determined for the catalysts later)
y = H_2 TCD area, in µVs
a = slope
b = noise of H_2 TCD area without hydrogen, in µVs

Calibration establishes the values of *a* (the constant of proportionality, or slope) and *b* (noise correction) in equation 1. The area of the observed H_2 peak in the TCD or FID trace can be converted, using equation 1, into the concentration of H_2 in $\mu L L^{-1}$ ($\mu L_{H2}.L^{-1}$). The flow rate of the argon vector gas is known, so the rate of H_2 or CO generation can be readily calculated using equation 2:

Rate of production of H_2 ($\mu L_{H2}.min^{-1}$) = [H_2 standard] ($\mu L_{H2}.L^{-1}$) x Ar flow rate ($L.min^{-1}$) (eq 2)

The ideal gas law (eq 3) then permits the conversion of volume of H_2 in L to the amount of substance in mol:

$$PV = nRT \quad \leftrightarrow \quad n = PV/RT \qquad \text{(eq 3)}$$

P = pressure = 1 atm
T = temperature = 298 K
R = ideal gas constant = 0.082 $L.atm.K^{-1}.mol^{-1}$
V = volume of hydrogen in L
n = amount of hydrogen in mol

The errors associated to the TON and TOF are estimated to be 10%

Hydrogen quantum yield

The absolute hydrogen quantum yield in % for the 395 nm and 445 nm LED is calculated at the maximum TOF of the photosensitizer Φ_{rH2} and for all the photons irradiating the system during all the photoreaction time Φ_{H2} using the following equations:

$$\Phi_{rH2} = 100 \times 2\frac{r_{H2}}{F}$$

$$\Phi_{H2} = 100 \times 2\frac{n_{H2}}{PhT}$$

$r_{H2} =$ rate of H_2 in $mol.s^{-1}$

The total photon flux (F, in $E.s^{-1}$) irradiating the bottom of the vial was determined using the following equation:

$$F = \frac{P \times \lambda}{C \times h}$$

where P is the power of the irradiation source measured with a power-meter, h is Planck's constant (6.626×10^{-34} J s^{-1}), c is the speed of light (3.00×10^{8} m s^{-1}) and l is the irradiation wavelength, taken as the maximum of the LED emission spectra.

n_{H2}= total amount of substance of H_2 in mol

$PhT = total\ amount\ of\ substance\ of\ photons\ irradiating\ the\ system\ in\ mol$.

Synthetic procedures

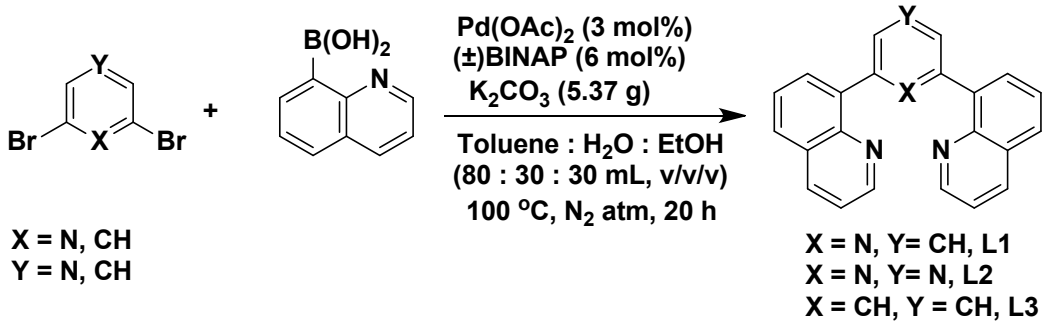

Scheme S1. Synthesis of Ligands 2,6-di(quinolin-8-yl)pyridine (**L1**), 2,6-di(quinolin-8-yl)pyrazine (**L2**) and 2,6-di(quinolin-8-yl)benzene (**L3**).

Ligands **L1**-**L3** were synthesized by Suzuki-Miyaura C-C bond-forming reaction of 2,6-dibromo-pyridine/pyrazine/phenyl and 8-quinolinylboronic acid in a yield of 50-85%.[15] The formation of the lignads was confirmed by their ^{1}H NMR analysis which matched with the literature reports.[15, 16]

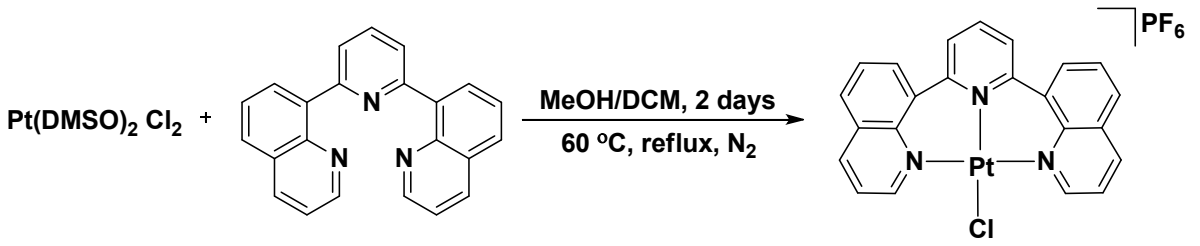

Scheme S2. Synthesis of 2,6-di(quinolin-8-yl)pyridine chloro platinum (II) hexafluorophosphate (**R1**).

Complexe **R1** was synthesized according to the literature procedure.[17] A Schlenk tube was charged with ligand **L1** (66.68 mg, 0.2 mmol, 1 equiv.) to which 2-3 ml of DCM was added. The reaction mixture was stirred at room temperature for 5-10 minutes until whole of the ligand was completely dissolved. To this was added Pt $(DMSO)_2Cl_2$ (100 mg, 0.23 mmol, 1.2 equiv.) and 4-5 ml of methanol. The reaction was purged with nitrogen via 10 evacuating and backfilling cycles of vacuum and nitrogen, respectively. The reaction mixture was refluxed for 2 days under nitrogen atmosphere and the precipitates obtained were collected via centrifugation, washed with diethyl ether and dried under vacuum. Cream coloured precipitates were obtained. Yield = 71% (75 mg). ^{1}H NMR (500 MHz, DMSO-d_6) δ 9.24 (d, J = 5.4 Hz, 2H), 9.00 (d, J = 8.2 Hz, 2H), 8.90 (d, J = 7.5 Hz, 2H), 8.52 (d, J = 8.2 Hz, 2H), 8.47 (t, J = 8.0 Hz, 1H), 8.31 (d, J = 8.1 Hz, 2H), 8.08 (t, J = 7.7 Hz, 2H), 7.80 (dd, J = 7.9, 5.7 Hz, 2H). ^{13}C NMR (126 MHz, DMSO-d_6) δ 157.88, 150.39, 141.71, 141.40, 141.00, 133.81, 132.39, 132.17, 128.86, 128.34, 127.59, 123.01. HRMS m/z = 564. 0652 [M-PF_6 + H + e]. ($C_{23}H_{16}ClN_3Pt$ requires 564.0680, difference in ppm = - 4.96, 100%). ATR-FTIR ($\tilde{\upsilon}$/cm^{-1}) C-H stretching (w, 3103-2978 cm^{-1}), C=C and C=N stretching (m, 1600-1506 cm^{-1}), C-H in plane bending (m, 1120-1032 cm^{-1}) and C-H out of plane bending (s, 831-761 cm^{-1}). M.P.- 253 °C (dec.).

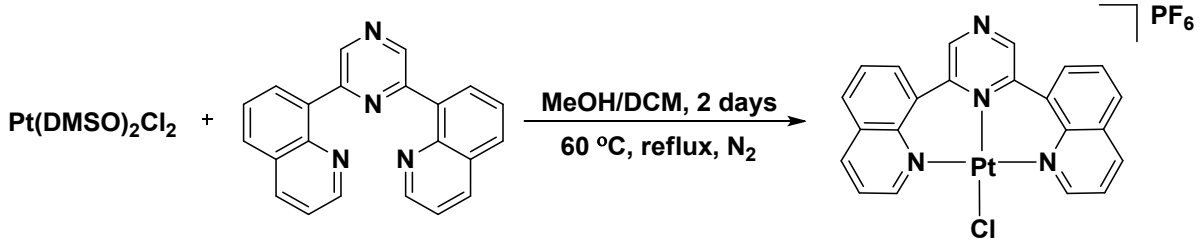

Scheme S3. Synthesis of 2,6-di(quinolin-8-yl)pyrazine chloro platinum (II) hexafluorophosphate (**1**)

A novel complex **1** was synthesized by adopting the literature procedure that was used for synthesizing **R1**.[17] A Schlenk tube was charged with ligand **L2** (67 mg, 0.2 mmol, 1 equiv.) to which 2-3 ml of DCM was added. The reaction mixture was stirred at room temperature for 5-

10 minutes until the whole of the ligand was completely dissolved. To this was added Pt $(DMSO)_2Cl_2$ (100 mg, 0.23 mmol, 1.2 equiv.) and 4-5 ml of methanol. The reaction was purged with nitrogen via 10 evacuating and backfilling cycles of vacuum and nitrogen, respectively. The reaction mixture was refluxed for 2 days under a nitrogen atmosphere and the precipitates obtained were collected via centrifugation, washed with diethyl ether and dried under vacuum. Pale-yellow precipitates were obtained. Yield = 72% (76 mg). ^{1}H NMR (500 MHz, $CDCl_3$) δ 9.78 (s, 2H), 9.10 (dd, J = 4.2, 1.8 Hz, 2H), 8.44 (dd, J = 7.3, 1.5 Hz, 2H), 8.28 (dd, J = 8.3, 1.8 Hz, 2H), 8.00 (dd, J = 8.2, 1.5 Hz, 2H), 7.72 (dd, J = 8.1, 7.2 Hz, 2H), 7.53 (dd, J = 8.3, 4.2 Hz, 2H). ^{13}C NMR (126 MHz, $CDCl_3$) δ 154.03, 151.02, 146.28, 145.26, 136.71, 133.67, 132.00, 130.85, 128.57, 126.61, 121.80. 135-DEPT NMR (126 MHz, $CDCl_3$) δ 165.67, 160.93, 151.38, 146.66, 145.51, 141.27, 136.46. HRMS m/z = 565. 0574 [M-PF_6 + H + e] ($C_{22}H_{15}ClN_4Pt$ requires 565.0633, difference in ppm = -10.44). ATR-FTIR ($\bar{\upsilon}$/cm^{-1}) C-H stretching (w, 2950-2854 cm^{-1}), C=C and C=N stretching (m, 1572-1506 cm^{-1}), C-H in plane bending (m, 1032-1026 cm^{-1}) and C-H out of plane bending (s, 831-788 cm^{-1}). M.P.- 251 ^{o}C (dec.).

Synthesis of 2,6-di(quinolin-8-yl)benzene chloro platinum (II) hexafluorophosphate (R2)

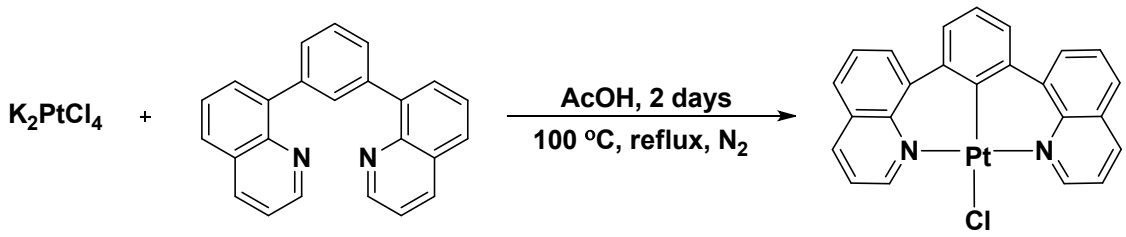

Scheme S4. Synthesis of 2,6-di(quinolin-8-yl)benzene chloro platinum (II) hexafluorophosphate (**R2**).

The complex **R2** was synthesized according to the literature procedure.[18] A Schlenk tube was charged with ligand **L3** (50 mg, 0.15 mmol, 1 equiv.) to which 5 mL of acetic acid was added. The reaction mixture was stirred at room temperature for 5-10 minutes until whole of the ligand was completely dissolved. To this was added of K_2PtCl_4. (75 mg, 0.18 mmol, 1.2 equiv.). The reaction was purged with nitrogen via 10-evacuating and backfilling cycles of vacuum and nitrogen, respectively. The reaction mixture was refluxed for 2 days at 100 °C under nitrogen atmosphere and the precipitates obtained were collected via centrifugation, washed with diethyl ether and dried under vacuum. Dark yellow colour precipitates were obtained for **R2**. Yield = 81% (80 mg). ^{1}H NMR (500 MHz, $CDCl_3$) δ 9.74 (dd, J = 5.3, 1.6 Hz, 2H), 8.38 (ddd, J = 13.0, 7.8, 1.5 Hz, 4H), 7.85 (dd, J = 8.1, 1.4 Hz, 2H), 7.71 (dd, J = 8.1, 7.3 Hz, 2H), 7.57 (d, J = 7.7

Hz, 2H), 7.37 – 7.31 (m, 3H). ^{13}C NMR (126 MHz, $CDCl_3$) δ 156.58, 142.15, 140.72, 138.74, 134.44, 128.89, 128.48, 128.29, 127.82, 126.87, 126.63, 125.47, 120.82. HRMS m/z = 526.0876 $[M\text{-}Cl]^+$ ($C_{24}H_{13}N_2Pt$ requires 526.0883, difference in ppm = -1.33, 100%). ATR-FTIR ($\bar{\upsilon}$/cm^{-1}) C-H stretching (w, 3045-2850 cm^{-1}), C=C and C=N stretching (m, 1621-1496 cm^{-1}) and C-H out of plane bending (s, 827-729 cm^{-1}). M.P.- 245 °C (dec.).

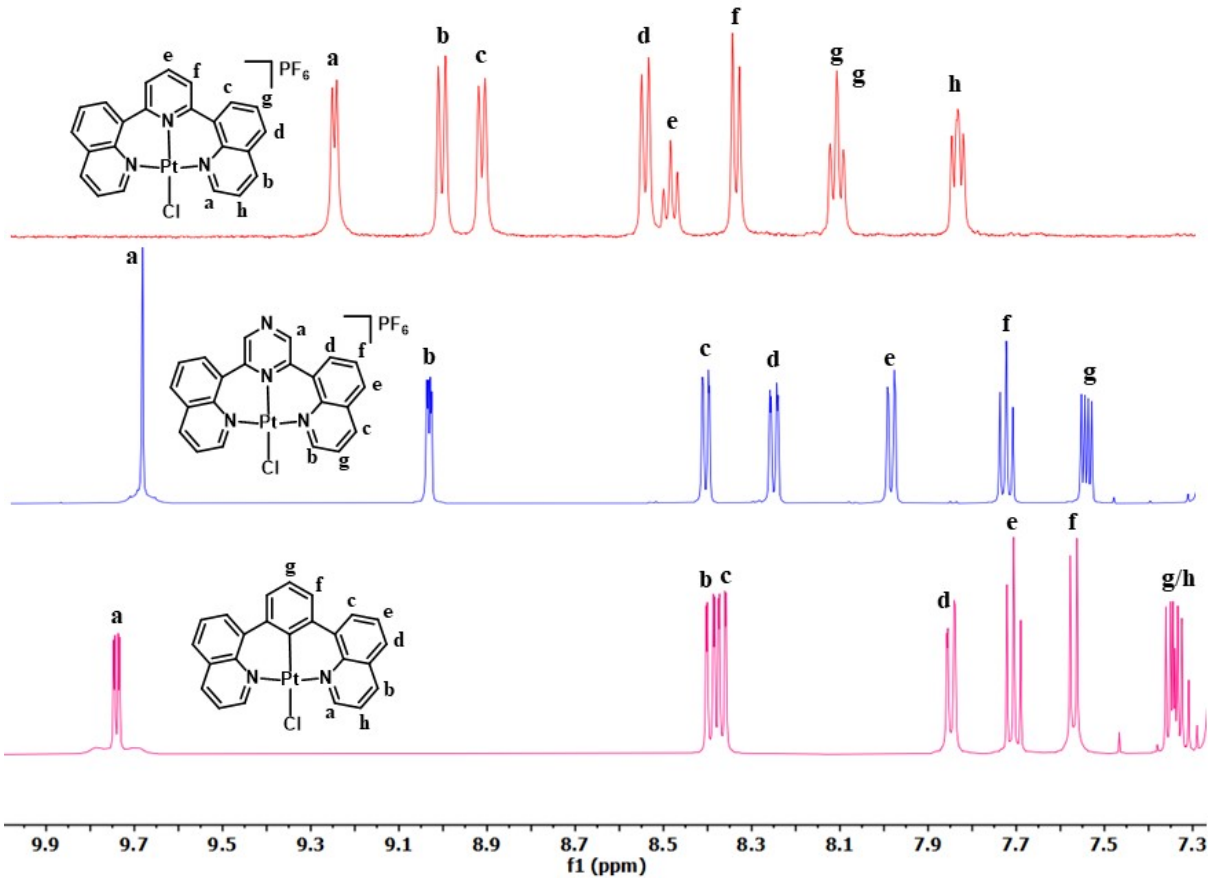

Fig S1. COSY interpreted 1H-NMR of **R1** in DMSO–d_6 and **1** and **R2** in $CDCl_3$ at 500 MHz at room temperature.

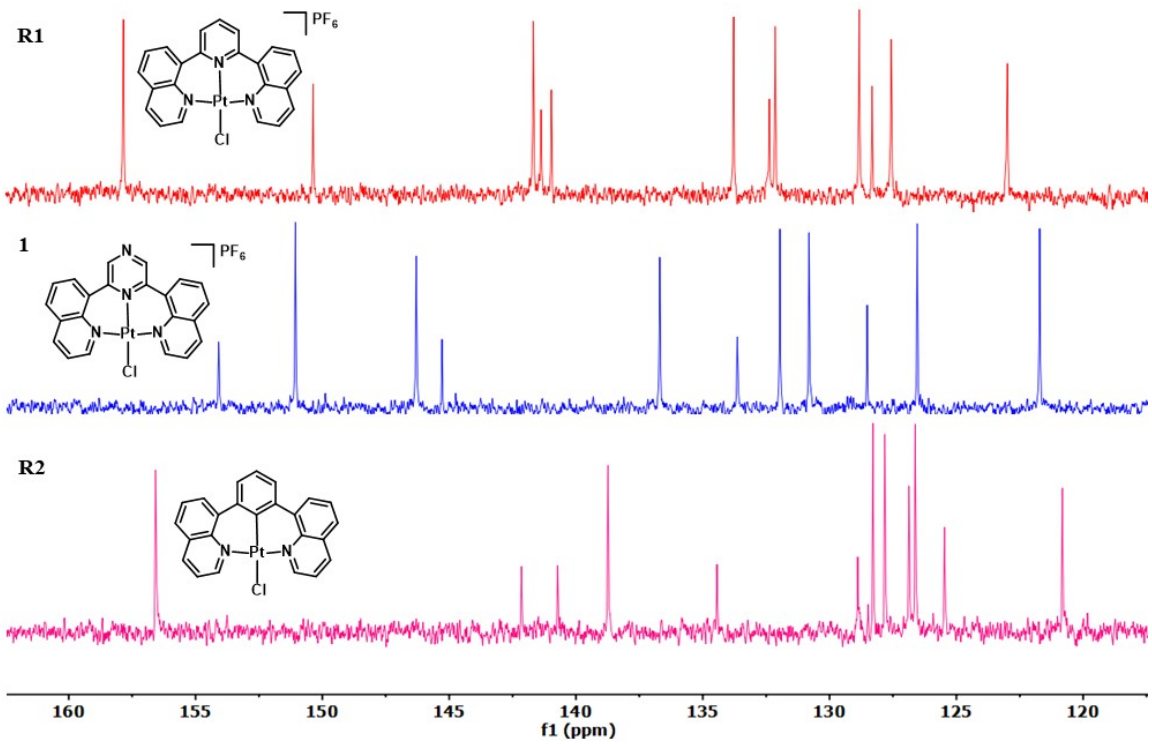

Fig S2. Stacked ^{13}C-NMR of **R1** in DMSO–d_6 and **1** and **R2** in $CDCl_3$ at 500 MHz at room temperature.

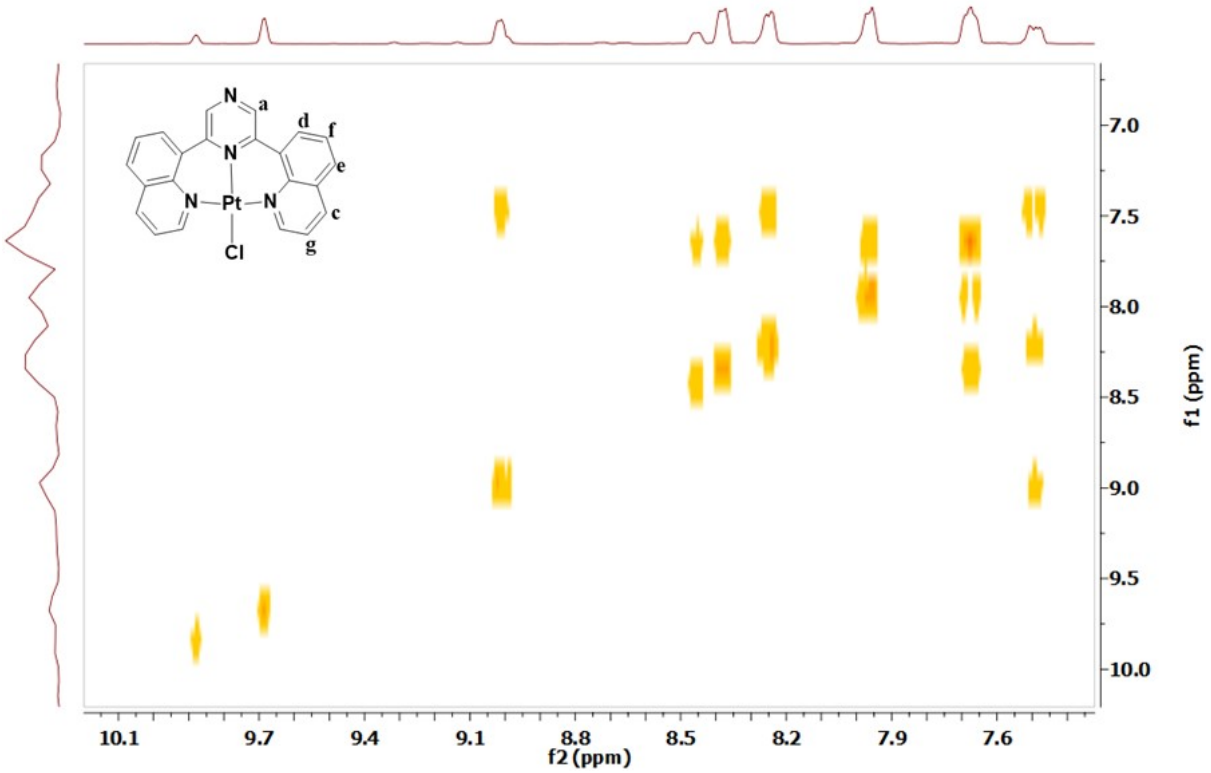

Fig S3. ^{1}H-^{1}H COSY NMR of **1** at RT in $CDCl_3$ at 500 MHz.

XPS Data

XPS data for all the three complexes **R1**, **1** and **R2** is given in the **Table S1**. The survey spectra of all the complexes along with the deconvoluted spectra are shown in **Fig S4-S6**. Deconvolution of the Pt 4f peaks in XPS showed the presence of two peaks in **R1** and **1** and three peaks in **R2** which could be attributed to presence of two types of bonding environment in **R1** and **1** (Pt-N and Pt-Cl) and three types of bonding environment in **R2** (Pt-N, Pt-C and Pt-Cl). The peaks in the range of 72-73 eV were assigned as $Pt4f_{7/2}$ whereas those in the range of 74-77 eV were assigned as Pt $4f_{5/2.}$ on the basis of the literature survey.[19, 20] Based on the data obtained and earlier literature reports the oxidation state of the Pt was found to be +2, the data also supported the existence of no Pt(0) in any of the complexes.[21] A comparison of the binding energy among the Pt $4f_{7/2}$ peaks for **R1** (Pt $4f_{7/2}$ =73.11 eV), **1**(Pt $4f_{7/2}$ =72.62 eV) and **R2** (Pt $4f_{7/2}$ =72.27 eV) revealed the fact that $Pt4f_{7/2}$ in **R2** had the lowest binding energy which might be attributed to the larger electron density on the Pt because of the cyclometalated carbon. The XPS spectra of the Cl 2p was observed as doublet (Cl $2p_{3/2}$ and Cl $2p_{1/2}$) in a ratio of 2:1 of in case of each of the complexes. The observed value of the binding energies was found to be in the range of 197.85- 199.79 eV revealing its presence as inorganic chloride (i.e. bound to Pt metal).[22] Deconvolution of the N 1s XPS spectra showed the presence of one peak in case of **R1** (N 1s = 400.34 eV) and **R2 (**N 1s = 400.06 eV) which might be attributed to the nitrogens bonded platinum.[19] However, deconvoluted XPS spectra of **1** (N 1s 399.98 eV) exhibited two peaks which showed the presence of two different types of nitrogen; one type included nitrogens bonded to Pt whereas the other one was the uncoordinated nitrogen present on the pyrazine ring.

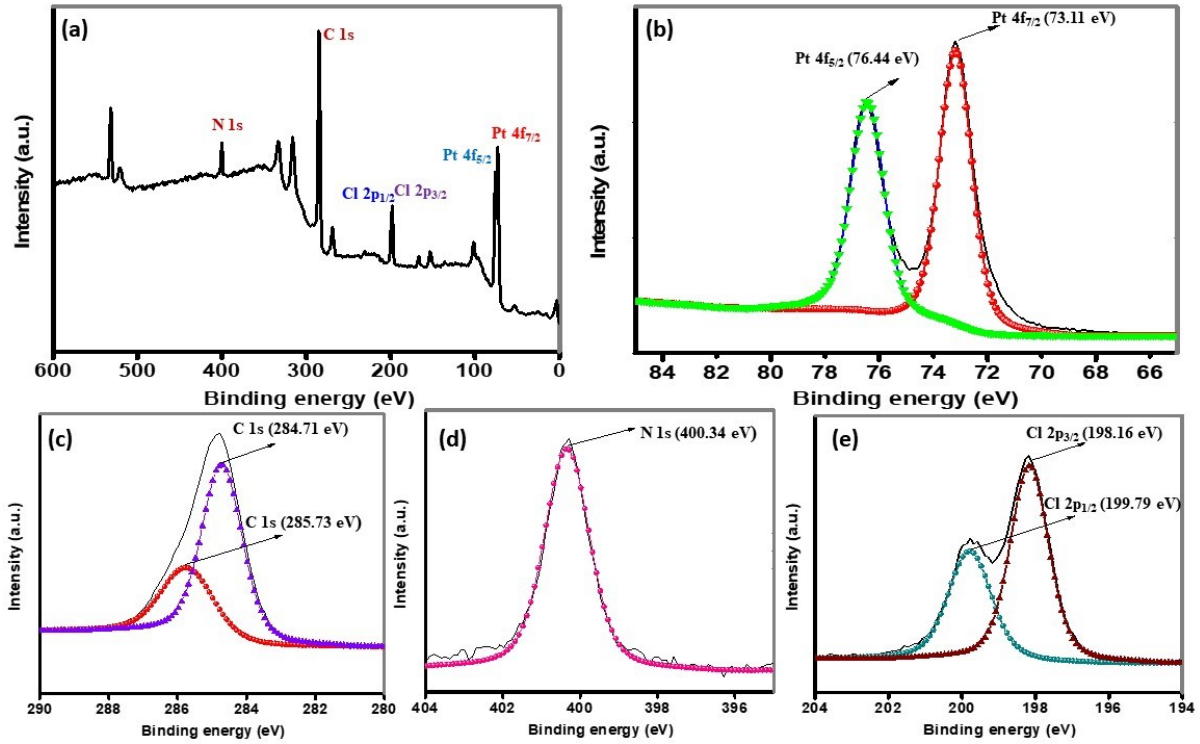

Fig S4. (a) XPS Survey spectra of **R1**, (b) deconvoluted XPS spectra of Pt 4f (c) deconvoluted XPS spectra of C 1s, (d) deconvoluted XPS spectra of N 1s and (e) deconvoluted XPS spectra of Cl 2p.

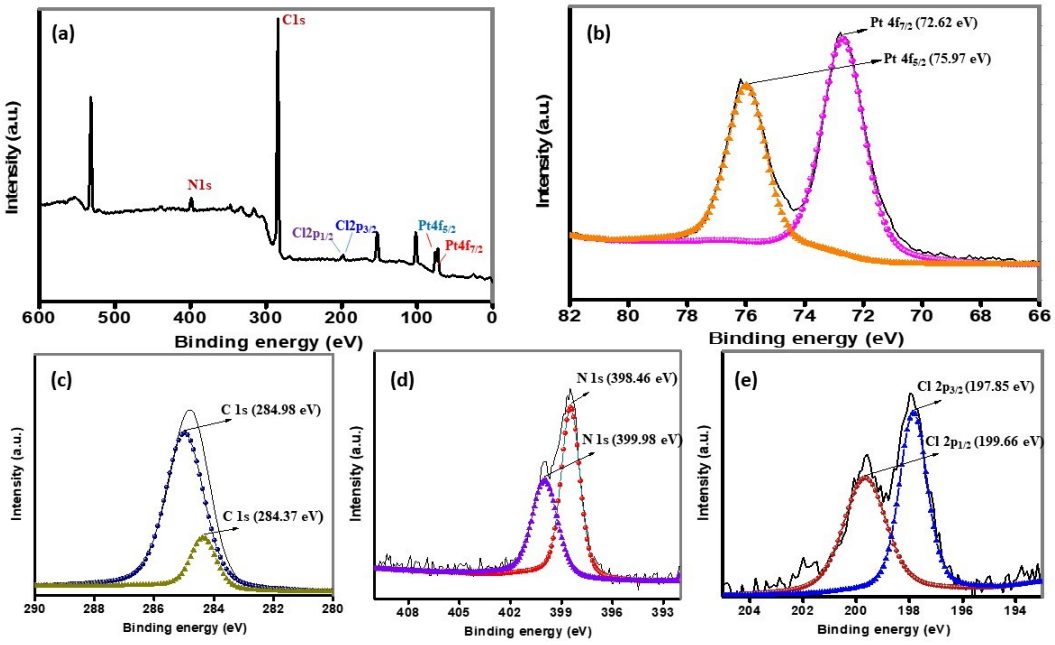

Fig S5. (a) XPS Survey spectra of **1**, (b) deconvoluted XPS spectra of Pt 4f (c) deconvoluted XPS spectra of C 1s, (d) deconvoluted XPS spectra of N 1s and (e) deconvoluted XPS spectra of Cl 2p.

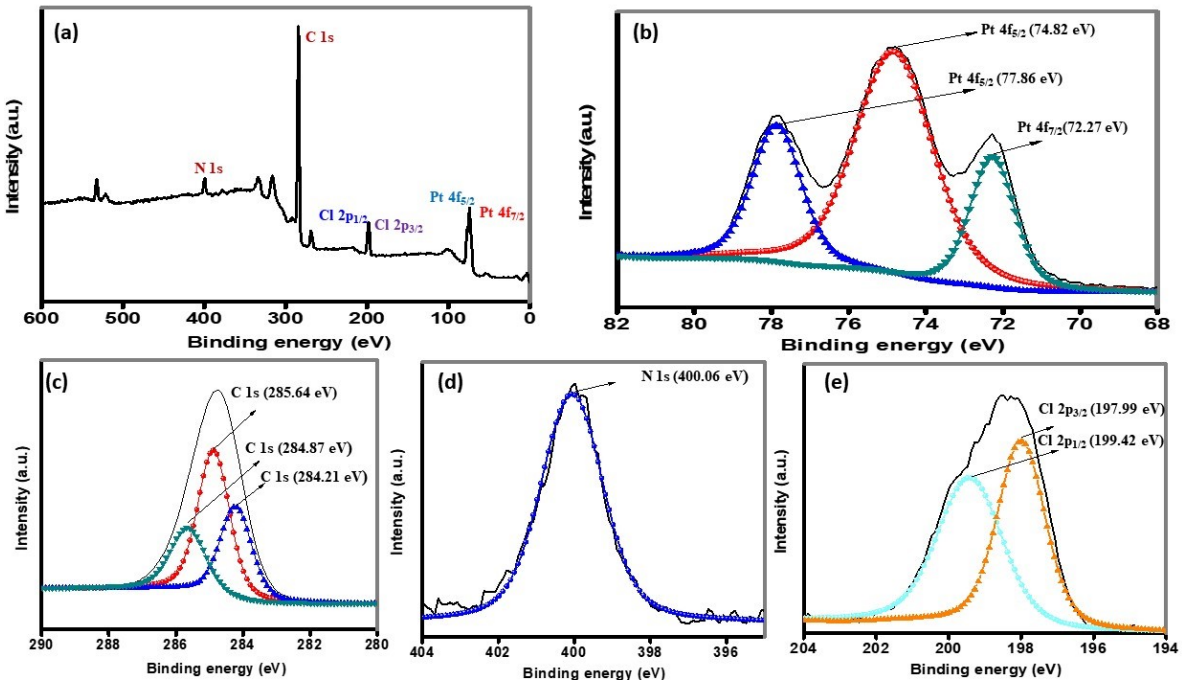

Fig S6. (a) XPS Survey spectra of **R2**, (b) deconvoluted XPS spectra of Pt 4f (c) deconvoluted XPS spectra of C 1s, (d) deconvoluted XPS spectra of N 1s and (e) deconvoluted XPS spectra of Cl 2p.

Table S1. XPS data of **R1**, **1** and **R2** (values in parenthesis are the full width at half maxima).

Cmpd	**Binding Energy in electronvolt**					
	C 1s	**N 1s**	**Cl $2p_{3/2}$**	**Cl $2p_{1/2}$**	**Pt $4f_{7/2}$**	**Pt $4f_{5/2}$**
R1	284.71 (1.4), 285.73 (1.79)	400.34 (1.39)	198.16 (1.24)	199.79 (1.30)	73.11 (1.65)	76.11 (1.51)
1	284.37 (0.97), 284.98 (1.53)	398.46 (1.32), 399.98 (1.75)	197.85 (1.24)	199.66 (1.9)	72.62 (1.79)	75.97 (1.57)
R2	284.21 (1.13), 284.87 (1.13), 285.64 (1.27)	400.06 (1.94)	197.99 (1.56)	199.42 (2.12)	72.27 (1.38)	74.82(2.38), 77.86 (1.51)

IR spectroscopic studies

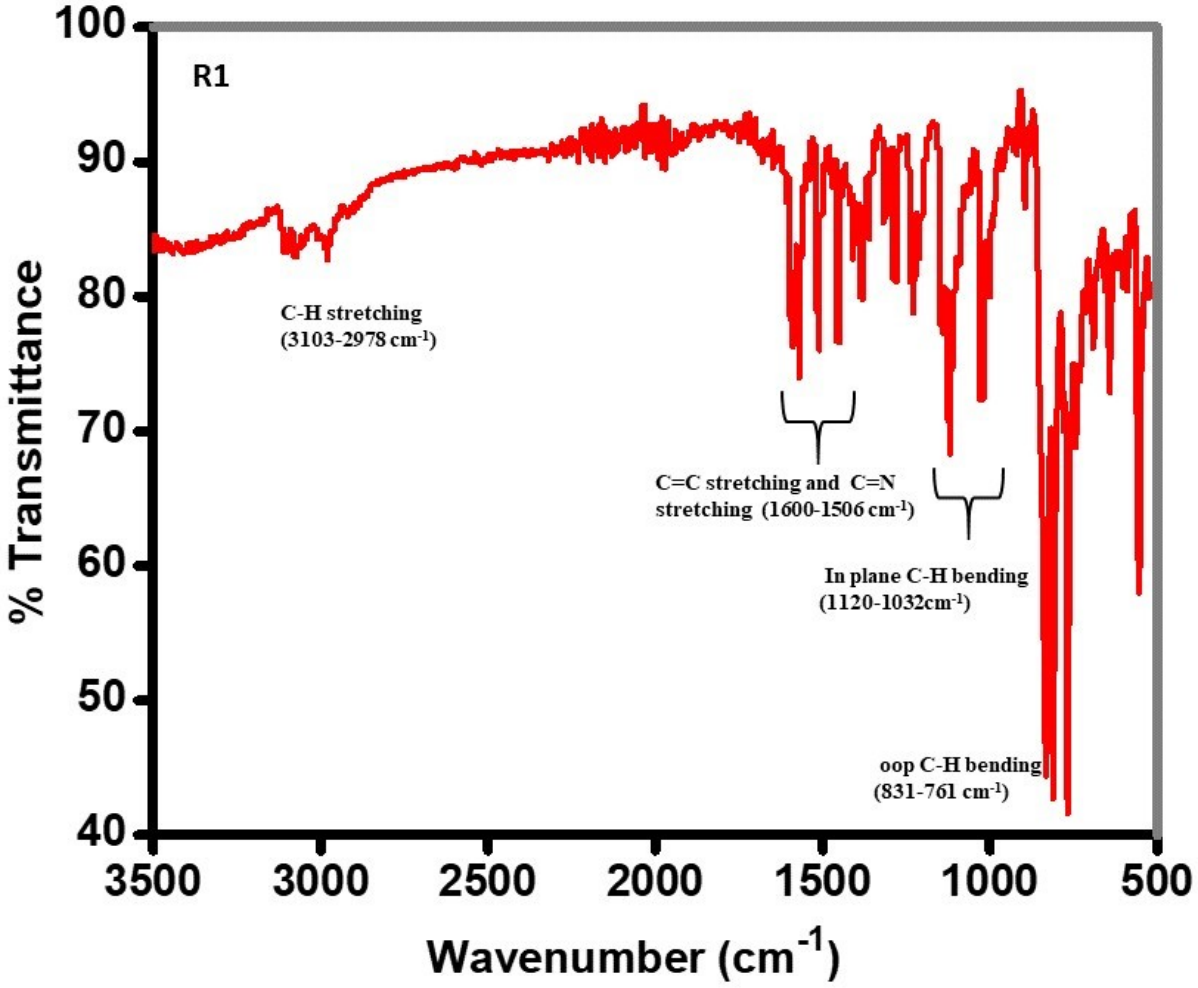

Fig S7. IR spectrum of **R1**. The presence of C-H, stretching, in-plane and out-of-plane bending frequencies, C=C stretching frequencies and C=N stretching frequencies showed the presence of the pyridine and quinoline rings in the structure.

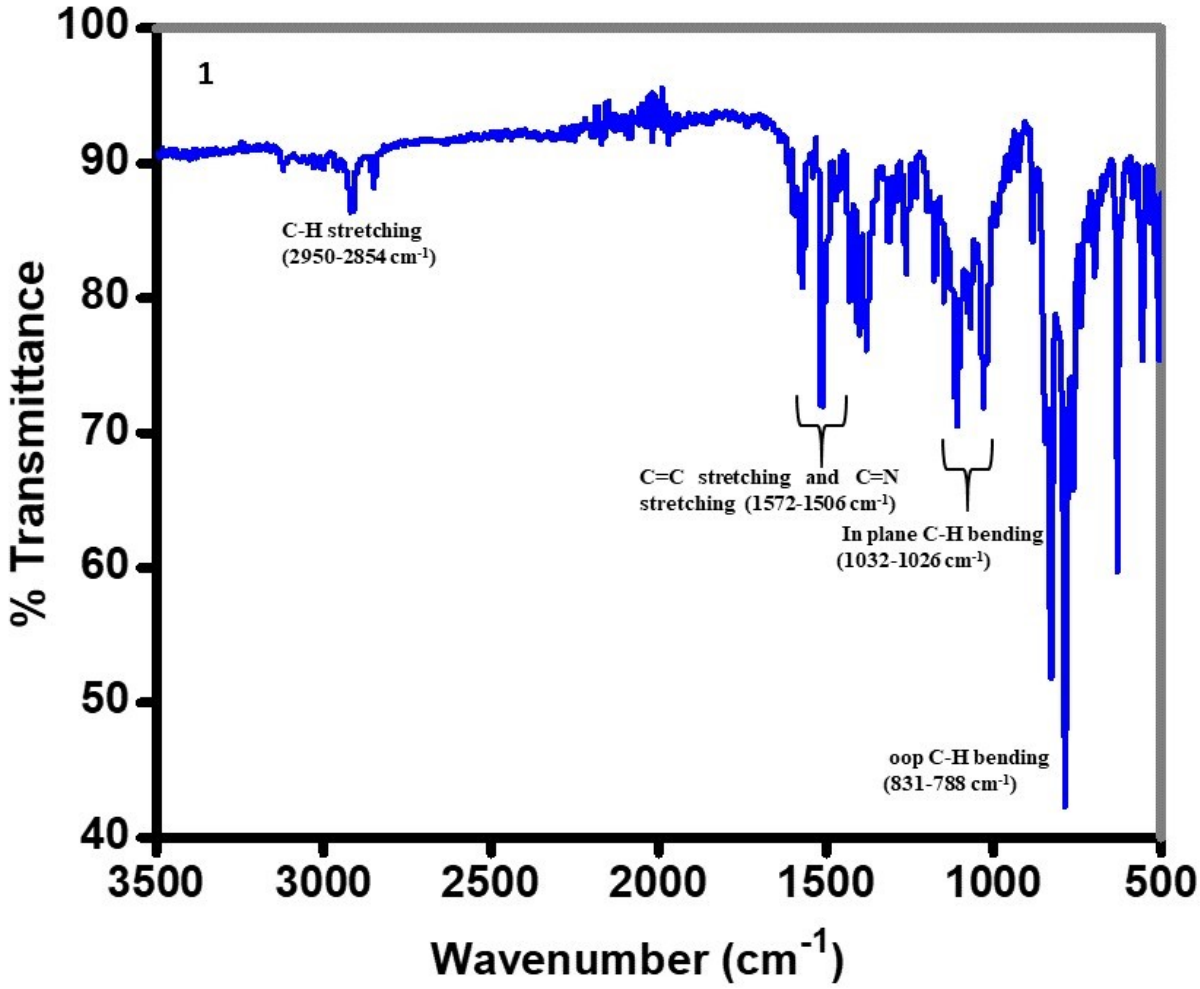

Fig S8. IR spectrum of **1**. The presence of C-H, stretching, in-plane and out-of-plane bending frequencies, C=C stretching frequencies and C=N stretching frequencies showed the presence of the pyrazine and quinoline rings in the structure.

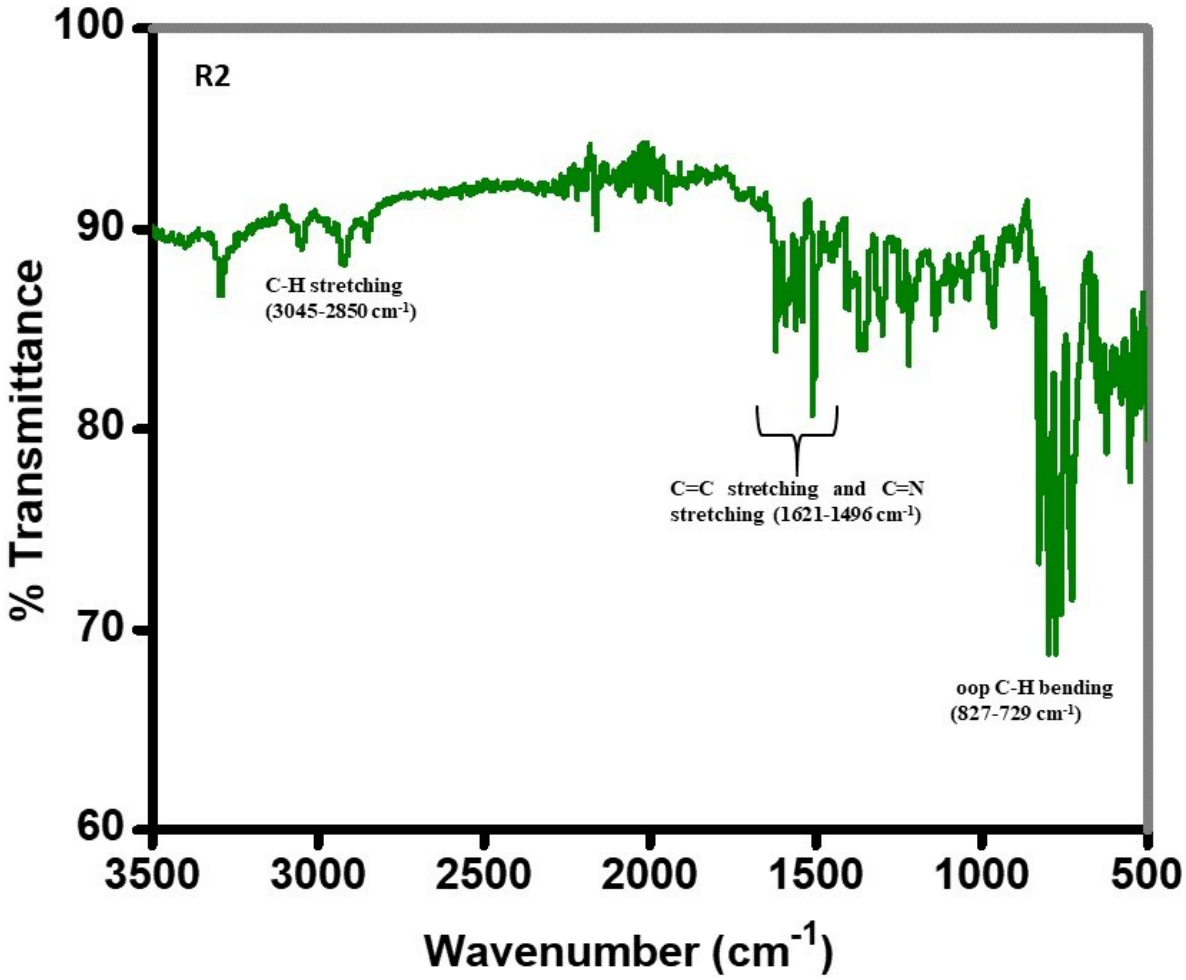

Fig S9. IR spectrum of **R2**. The presence of C-H, stretching and out-of-plane bending frequencies, C=C stretching frequencies and C=N stretching frequencies showed the presence of the benzene and quinoline rings in the structure.

Powder X-ray diffraction (PXRD) studies

Powder XRD measurement was carried for **R2** (**Fig S12**). The crystals of **R2** were grown by the slow diffusion of hexane into the concentrated solution of **R2** in DCM. Though the crystal could not be solved because of high disorder, it revealed the Pt to be in +2 oxidation state (also proved by XPS data). The crystals were grinded to give the power which was subjected to powder X-ray diffraction analysis. The experimentally obtained PXRD pattern was compared with the PXRD pattern obtained from the disordered crystal data of **R2** using Mercury software. Both the experimental and the simulated patterns were found to exhibit good agreement giving an indication that Pt was in +2 oxidation state in **R2** (**Fig S13**). Similarly, PXRD analysis of **R1** and **1** was also done. All the PXRD patterns were found to be almost similar giving medium to strong intensity peaks in the 2θ range of 5-40^{o} (**Fig S10-12**). All the three complexes were

found to be in monoclinic phase according to PXRD data. The other parameters obtained from the PXRD analysis are shown in **Table S2**.

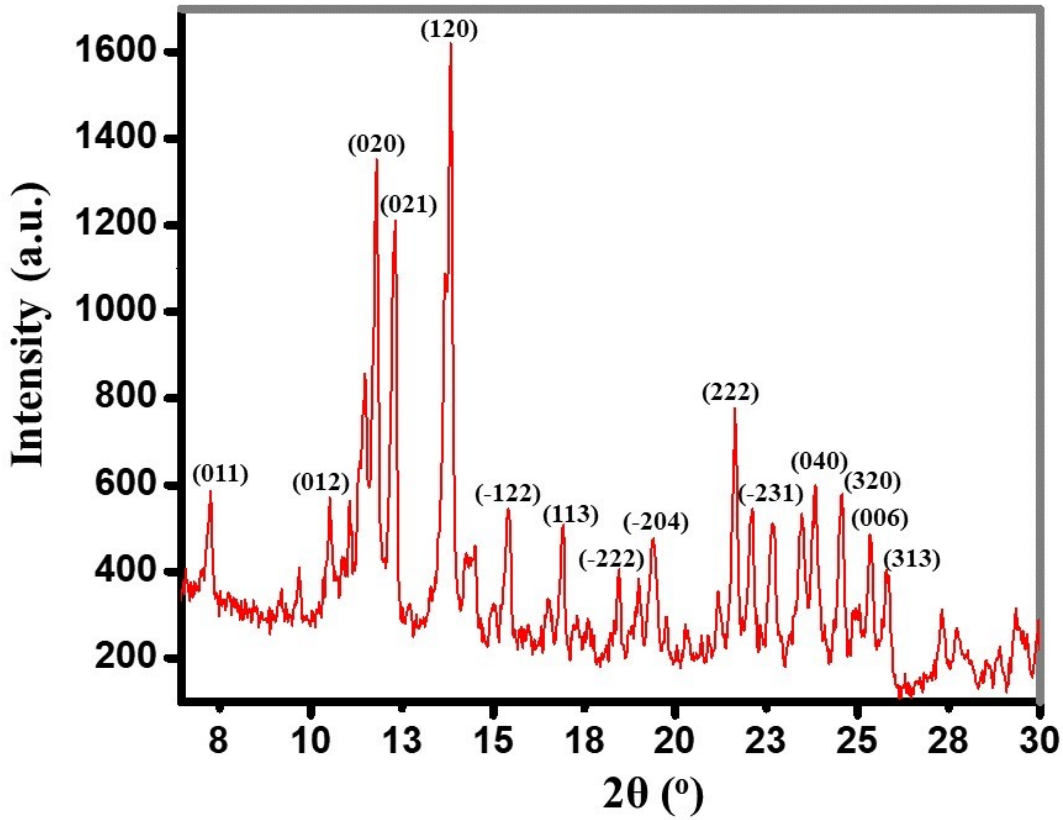

Fig S10. Powder X-ray diffraction pattern of **R1**.

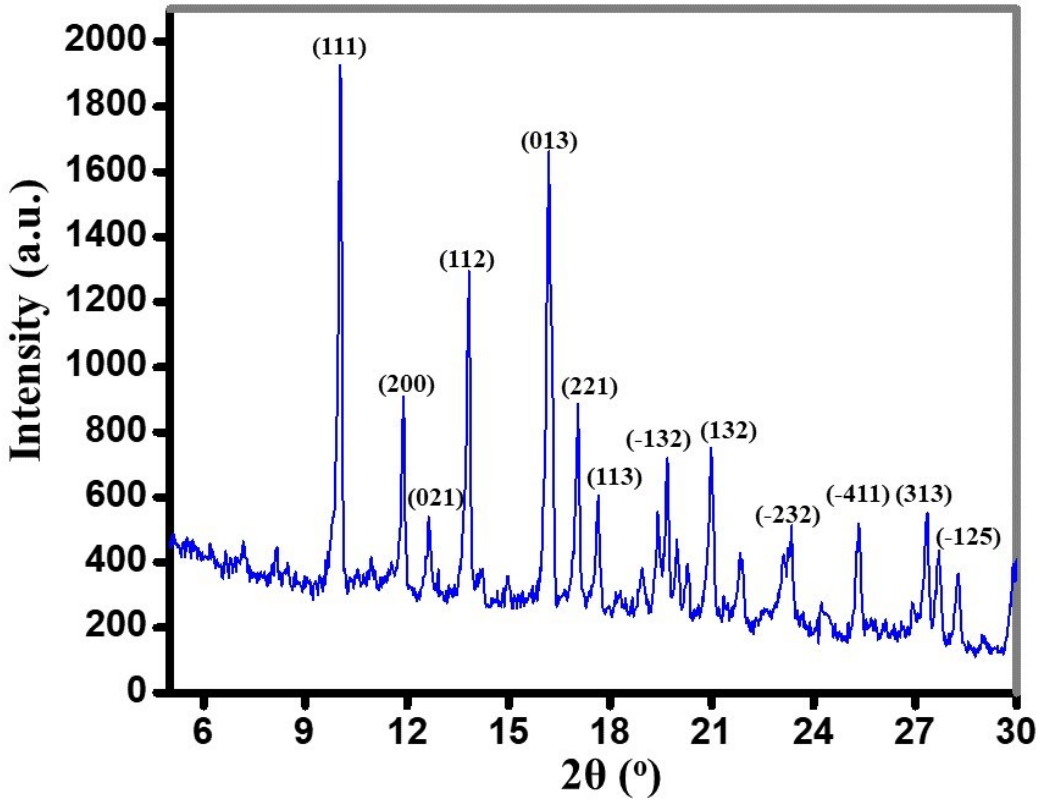

Fig S11. Powder X-ray diffraction pattern of **1**.

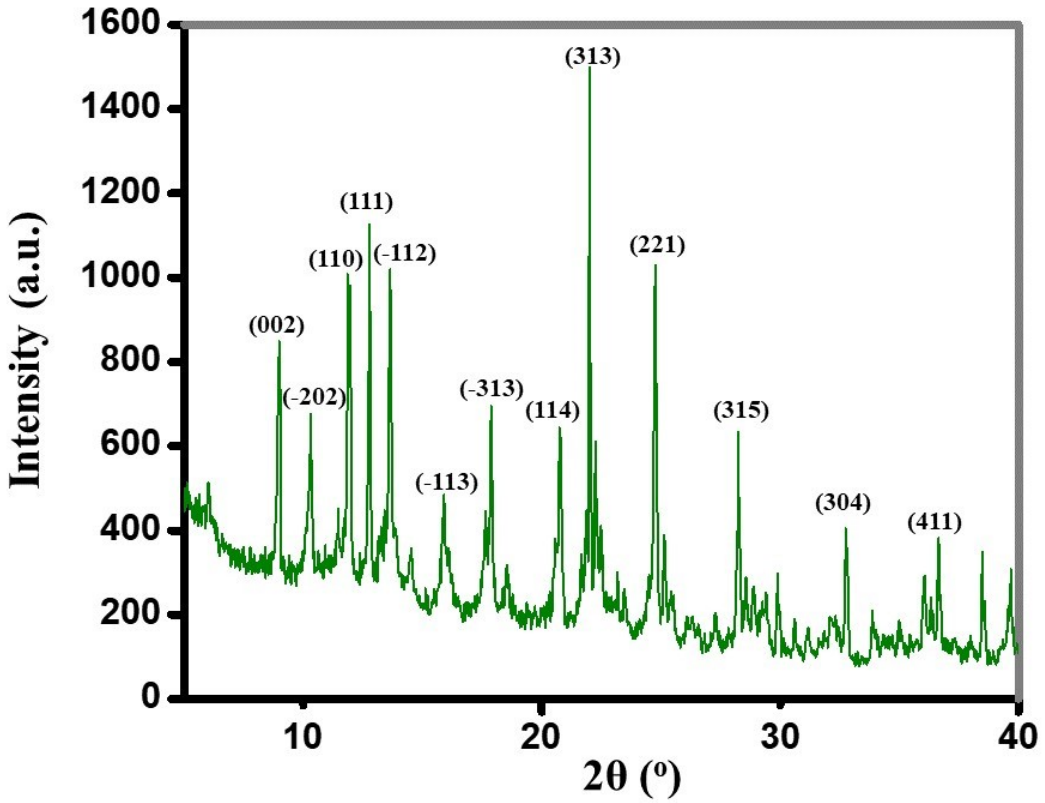

Fig S12. Powder X-ray diffraction pattern of **R2**.

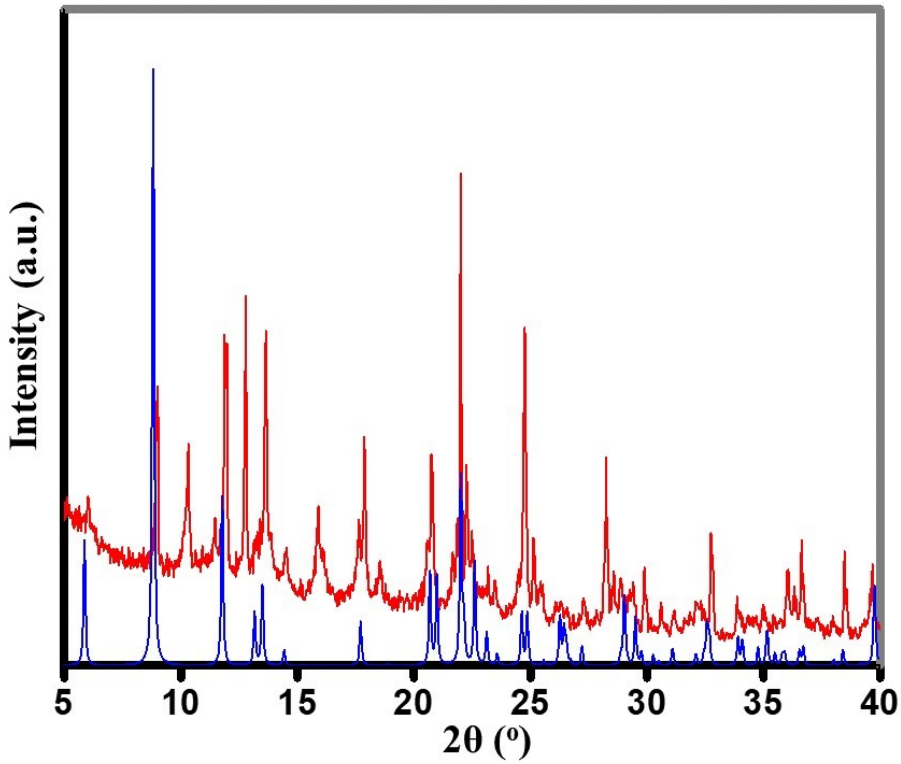

Fig S13. Experimental (red) and simulated (blue) (generated from the crystal data of disordered crystal of **R2**) PXRD pattern of **R2**.

Table S2. Cell parameters obtained from PXRD analysis.

Cmpd	Cell Parameters					
	a (Å)	b (Å)	c (Å)	α (°)	β (°)	γ (°)
R1	13.0470	15.0180	21.6600	90.0000	101.7700	90.0000
1	15.5910	15.9170	17.8070	90.0000	99.4500	90.0000
R2	23.8720	7.9160	23.4620	90.0000	106.9840	90.0000

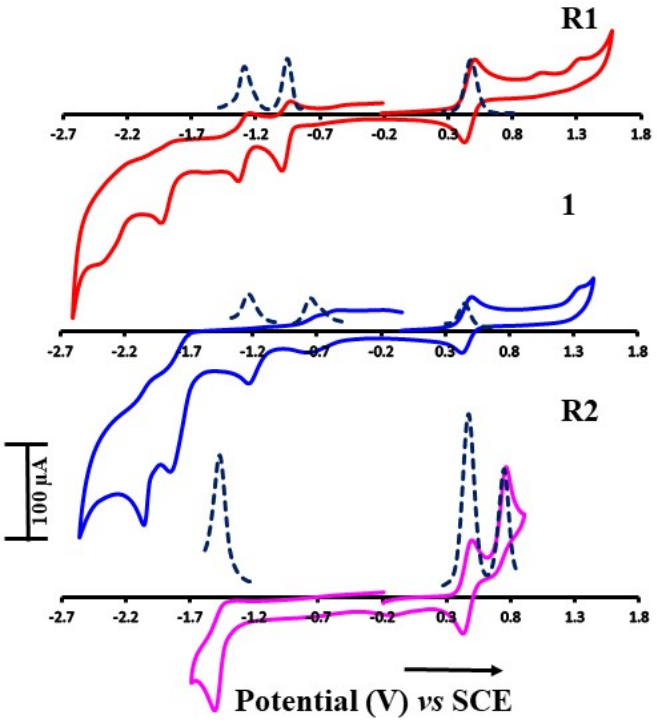

Fig S14. Cyclic voltammograms (solid) and square wave voltammograms (dotted) of complexes **R1**, **1** and **R2** in degassed DMF, recorded at a scan rate of 100 mV/s.

Table S3. Electrochemical data of **R1**, **1** and **R2** in DMF.

Cmpd	$E_{1/2}^{Ox/V}$ (mV)[a]	$E_{1/2}^{Red/V}$ (mV)[a]	ΔE_{redox}[b]	E_{HOMO} (eV)[c]	E_{LUMO} (eV)[c]	$\Delta E_{\lvert H-L \rvert}$ (eV)[c]
R1	-----	-0.97 (60), -1.30 (80), -1.89 (100), -2.31 (180)	-----	-9.21	-5.41	3.8
1	-----	-0.73 (80), -1.23 (irr)[d], -1.77 (150), -2.02 (60)	-----	-9.36	-5.74	3.62
R2	0.76 (irr)[d]	-1.51 (irr)[d]	2.27	-5.30	-2.05	3.25

[a]Potentials are in volts (V) *vs* SCE for DMF solution, 0.1 M in [n-Bu_4N]PF_6, recorded at room temperature at a sweep rate of 100 mV/s using a glassy carbon electrode as working electrode, a platinum wire as counter electrode and silver wire as a reference electrode. The difference between cathodic, E_{pc}, and anodic E_{pa}, peak potentials, ΔE_p (millivolts) is given in parenthesis. [b]ΔE_{redox} is the difference (in mV) between first oxidation and first reduction potentials. [c]DFT calculated energy in eV. [d]irreversible in nature.

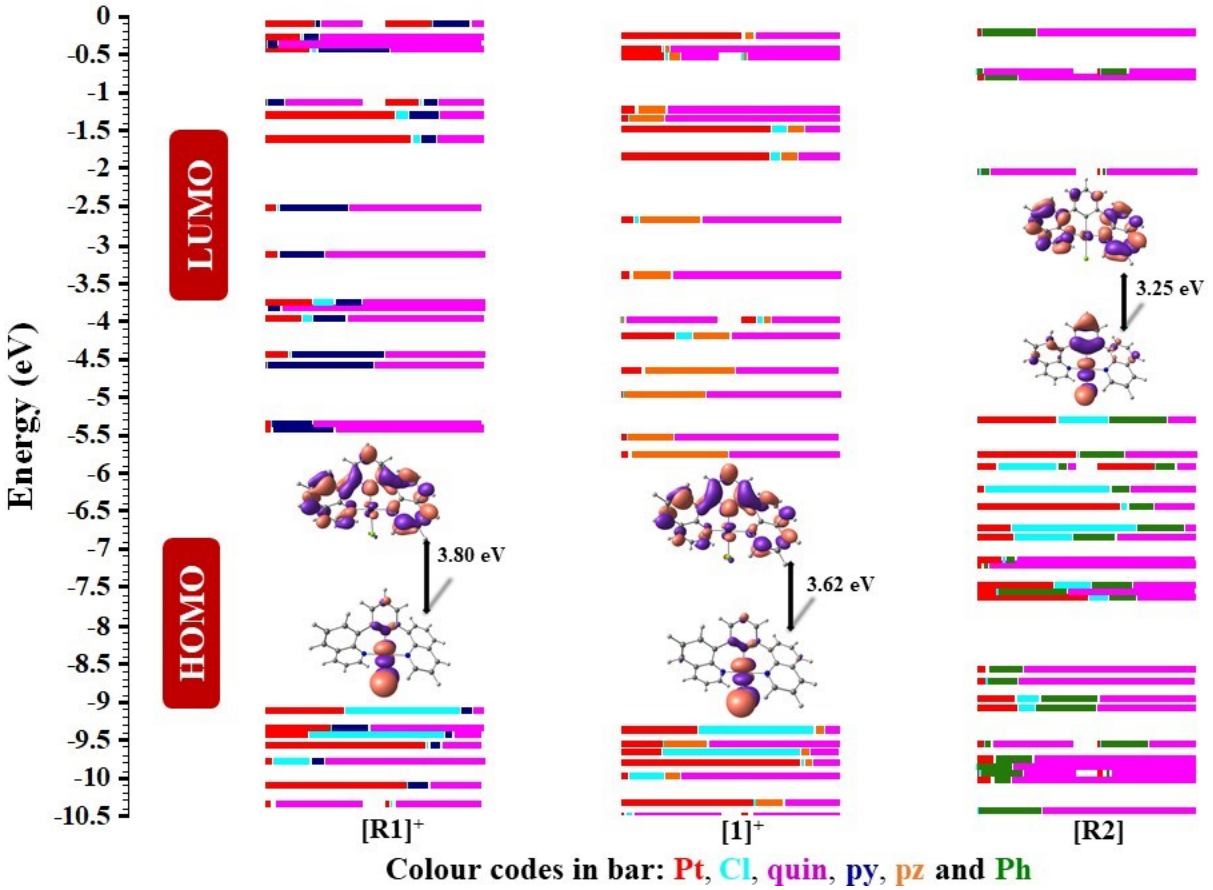

Fig S15. Calculated frontier MO energies of [**R1**]$^+$, [**1**]$^+$ and [**R2**] calculated from DFT [B3LYP/SBKJC-VDZ for Pt(II) and 6-31g** for C, H, N, Cl] and 0.05 eV threshold of degeneracy. Kohn-Sham MOs of [**R1**]$^+$, [**1**]$^+$ and [**R2**] are also shown.

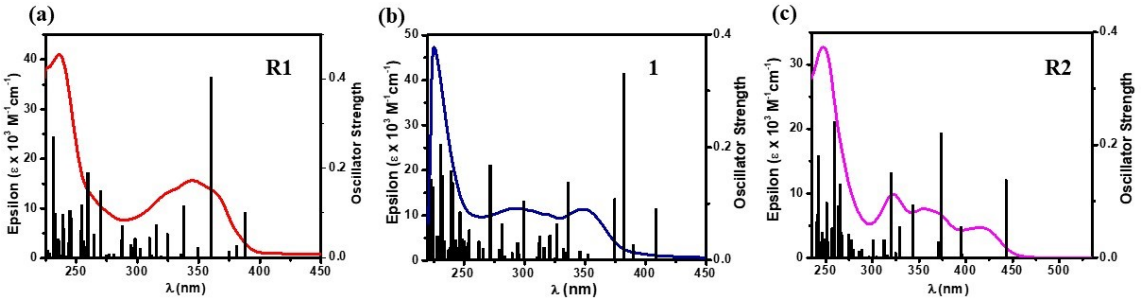

Fig S16. (**a**), (**b**) and (**c**) Overlay of the experimental UV-vis absorption spectra (curved lines) of the complexes with their predicted transition (vertical bars) calculated by singlet TD-DFT calculations [B3LYP/SBKJC-VDZ for Pt(II) and 6-31g** for C, H, N, Cl].

Table S4. UV-vis absorption data of **R1**, **1** and **R2** complexes.

Compound	**λ_{max}, nm (ε x 10^3, $M^{-1}cm^{-1}$)**[a]
R1	237 (41), 323 (13), 345 (16)
1	226 (47), 293 (11), 321 (10), 350 (11)
R2	247 (32), 322 (9), 355 (7), 418 (4)

Table S5. Selected transitions from TD-DFT calculations of [**R1**]$^+$ in the Singlet Ground State [B3LYP/SBKJC-VDZ for Pt(II) and 6-31g** for C, H, N, Cl].

λ_{abs}/nm (TD-DFT)	λ_{abs}/nm (ε x10^3 M^{-1}cm^{-1}) [expt.]	f (TD-DFT)	Major transition(s)	Character
231	237 (41)	0.2709	H-7→L+2 (24%), H-6→L+3 (18%), H-3→L+5 (31%),	quin(π)→quin(π^*) (major), quin(π)→Py(π^*) (minor), Pt(dπ)→quin(π^*) (minor)
324	323 (13)	0.0539	H-4→L+1 (23%), H-3→L+1 (60%)	Pt(dπ)→quin(π^*) (major), quin(π)→quin(π^*) (minor), quin(π)→Py(π^*) (minor)
337	345 (16)	0.115	H-2→L+12 (39%), H-1→L+3 (15%)	Cl$^-$(π)→quin(π^*) (major), quin(π)→quin(π^*) (minor), quin(π)→Py(π^*) (minor) Pt(dπ)→quin(π^*) (minor), Pt(dπ)→Py(π^*) (minor)

Table S6. Selected transitions from TD-DFT calculations of [**1**]$^+$ in the Singlet Ground State [B3LYP/SBKJC-VDZ for Pt(II) and 6-31g** for C, H, N, Cl].

λ_{abs}/nm (TD-DFT)	λ_{abs}/nm (ε x10^3 M^{-1}cm^{-1}) [expt.]	f (TD-DFT)	Major transition(s)	Character
232	226 (47)	0.2052	H-3→L+5 (70%)	quin(π)→quin(π^*) (major), quin(π)→Pz(π^*) (minor), Pt(dπ)→quin(π^*) (minor)
299	293 (11)	0.1046	H-6→L (29%), H-3→L+1 (10%), H-3→L+3 (20%), H-3→L+4 (19%)	quin(π)→quin(π^*) (major), quin(π)→Pz(π^*) (minor), Pt(dπ)→quin(π^*) (minor), Pt(dπ)→Pz(π^*) (minor)
336	321 (10)	0.1381	H-3→L+1 (75%)	Pt(dπ)→quin(π^*) (major), Pt(dπ →Pz(π^*) (minor)
374	350 (11)	0.1087	H-1→L+1 (83%)	quin(π)→quin(π^*) (major), Pt(dπ)→quin(π^*) (minor), Pt(dπ) →Pz(π^*) (minor), quin(π)→Pz(π^*) (minor)

Table S7. Selected transitions from TD-DFT calculations of [**R2**] in the Singlet Ground State [B3LYP/SBKJC-VDZ for Pt(II) and 6-31g** for C, H, N, Cl].

λ_{abs}/nm (TD-DFT)	λ_{abs}/nm (ε x10^3 M^{-1}cm^{-1}) [expt.]	f (TD-DFT)	Major transition(s)	Character
256	247 (32)	0.0528	H-2→L+5 (42%),	quin(π)→quin(π^*) (major), quin(π)→Ph(π^*) (minor), Pt(dπ)→quin(π^*) (minor)
320	322 (9)	0.1506	H-5→L (22%), H→L+2 (55%)	Pt(dπ)→quin(π^*) (major), Cl$^-$(π)→quin(π^*) (minor), Ph(π)→quin(π^*) (minor),

				quin(π)→quin(π*) (minor)
373	355 (7)	0.2212	H-2→L+1 (57%), H-1→L+1 (41%)	Pt(dπ)→quin(π*) (major), quin(π)→quin(π*) (minor), Ph(π) →quin(π*) (minor)
442	418 (4)	0.1385	HOMO→LUMO (98%)	Pt(dπ)→quin(π*) (major), Cl^-(π)→quin(π*) (minor), Ph(π)→quin(π*) (minor), quin(π)→quin(π*) (minor)

Chemical stabilities of the complexes

The chemical stability of the complexes **R1**, **1** and **R2** was assessed by monitoring the UV-visible absorption spectra of same solution of each of the complexes in DCM for seven continuous days (**Fig S17**). An inspection of the absorption spectra showed no change in the position of the ^{1}MLCT/^{1}ILCT/^{1}LC bands the assignment of which has already been done in the main manuscript. Though the complexes **R1** and **1** showed almost same value of the absorbance, the change in the absorbance of **R2** might be atributed to the change in concentration due to evaporation of DCM (the position was bands was still retained).This accounts for the chemical stabilty of the complexes in solution.

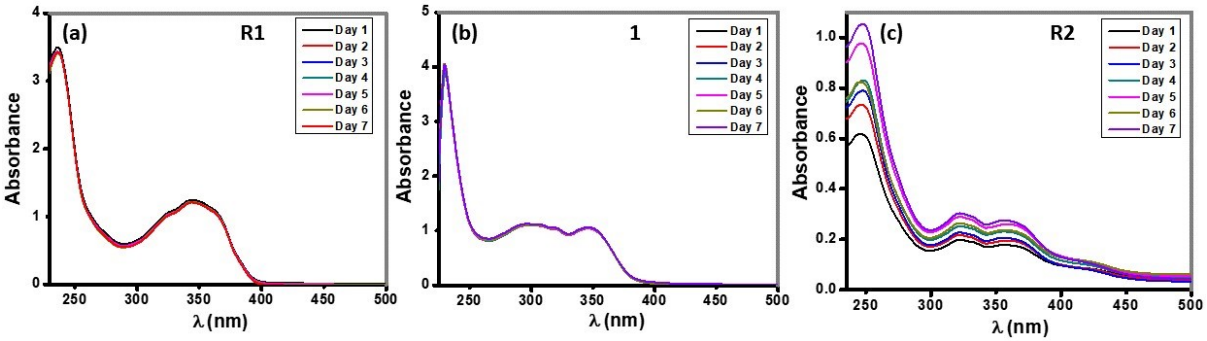

Fig S17. (a), (b) and (c) UV-vis absorption spectra of the complexes **R1**, **1** and **R2**, respectively in DCM over a period of seven continuous days.

Table S8. Photophysical data of **R1**,**1** and **R2** in degassed DCM at RT.

Cmpd	**Absorption (DCM)**	**Emission**[a]	
	λ_{abs}/nm (ε X 10^3/M^{-1} cm^{-1})	λ_{em}/nm (DCM)[b]	Φ_{PL}/%
R1	345	552	3.07
1	350	595	0.42
R3	418	601 (sh), 628	1.50

[a]Steady state emission spectra were recorded in degassed DCM, λ_{exc} = 380 nm. Solution's Φ_{PL} were measured using $[Ru(bpy)_3](PF_6)_2$ as an external reference (λ_{exc} = 380 nm in DCM, Φ_{PL} = 13%),[23] [b]at RT.

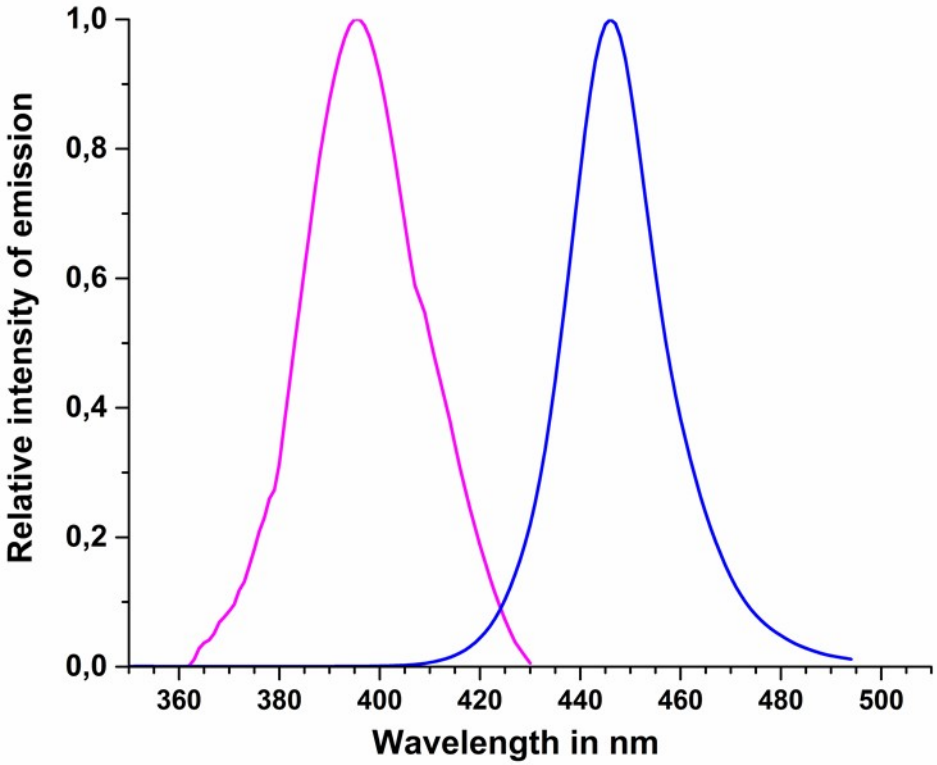

Fig S18. Emission spectra of light-emitting diodes used as irradiation sources for HER experiments (UV-LED and blue LED).

Table S9. Absolute QY (%) of hydrogen production for 396 nm and 445 nm LEDs.

	R1		**1**		**R2**	
	Φ_{rH2}	Φ_{H2}	Φ_{rH2}	Φ_{H2}	Φ_{rH2}	Φ_{H2}
Absolute QY (LED 396 nm)	17.7	0.67	3.85	0.047	3.85	0.43
Absolute QY (LED 445 nm)	8.46	0.81	10.3	1.07	4.36	0.47

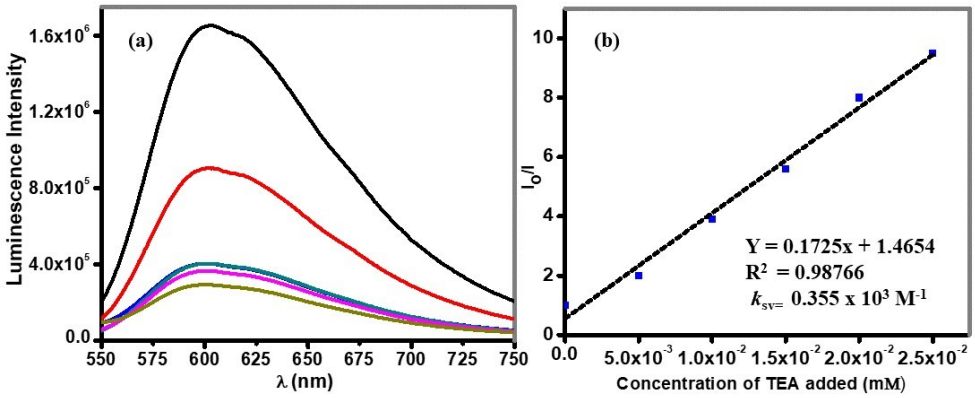

Fig S19. (a) Stern-Volmer plot of the emission quenching of $[Ru((bpy)_3]^{2+}$ solution (10^{-4} M) by TEA in DCM, (b) best-fit equation of the Stern-Volmer plot.

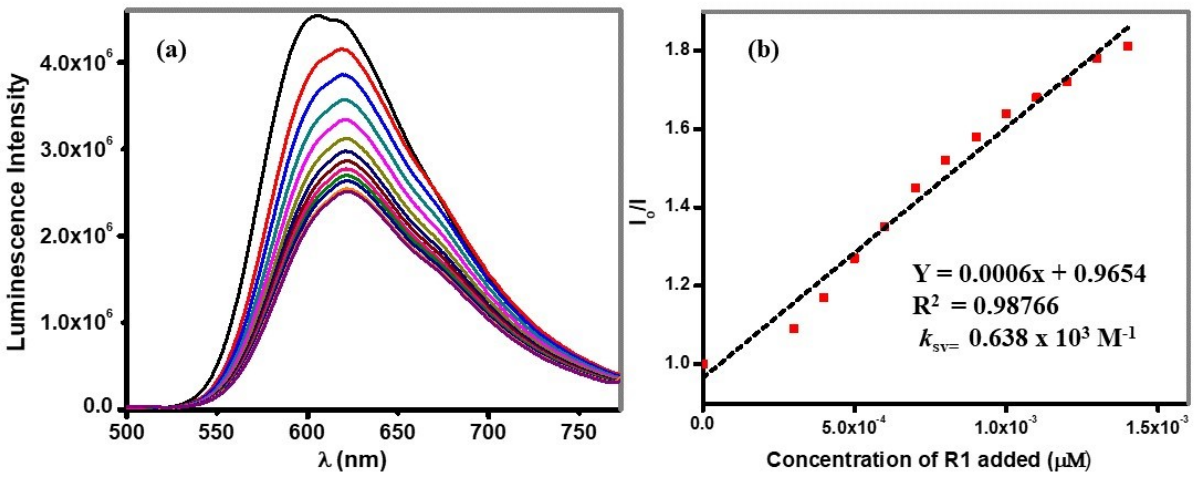

Fig S20. (a) Stern-Volmer plot of the emission quenching of $[Ru((bpy)_3]^{2+}$ solution (10^{-4} M) by **R1** in DCM, (b) best-fit equation of the Stern-Volmer plot.

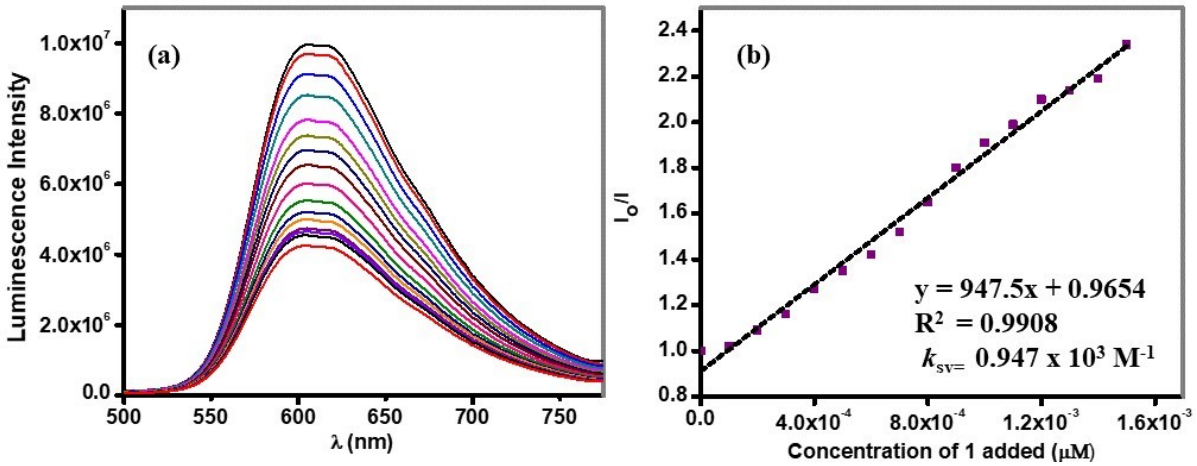

Fig S21. (a) Stern-Volmer plot of the emission quenching of $[Ru((bpy)_3]^{2+}$ solution (10^{-4} M) by **1** in DCM, (b) best-fit equation of the Stern-Volmer plot.

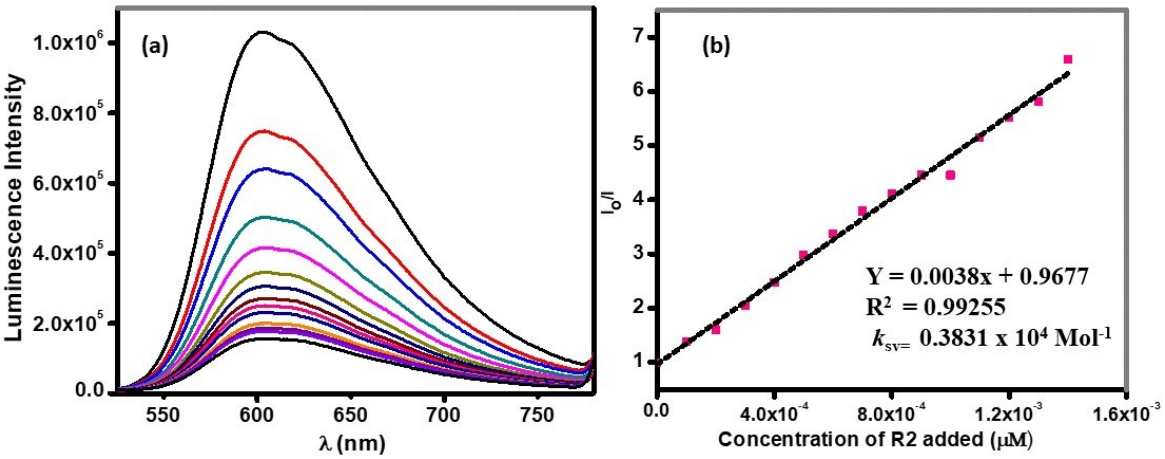

Fig S22. (a) Stern-Volmer plot of the emission quenching of $[Ru((bpy)_3]^{2+}$ solution (10^{-4} M) by **R2** in DCM, (b) best-fit equation of the Stern-Volmer plot.

Photoelectric properties

In order to interpret the photoelectric behaviour of the complexes, transient photocurrent responses of **R1** and **R2** under UV light irradiation were studied. In a typical procedure, complexes **R1** and **R2** were deposited on a stainless-steel piece which worked as working electrode whereas silver and platinum wires were used as reference and counter electrodes, respectively. **Fig S23** and **S24** show the generation of photocurrent for **R1** and **R2** when irradiated with UV light. The light was irradiated on the stainless-steel electrode after every one minute. As soon as the light was irradiated, an increase in current was observed, though the increase was not very much, still it was observable as can be seen from **Fig S23** and **S24**. The generation of the photocurrent was observed with good reproducibility indicating the fact that the electrodes formed by depositing **R1** and **R2** were stable and photocurrent response was quite reversible.[24] This photocurrent response was very much consistent with the photocatalytic hydrogen production activity which again gives an indication that as soon as the light was irradiated on the samples, it caused electron generation/transfer phenomenon.

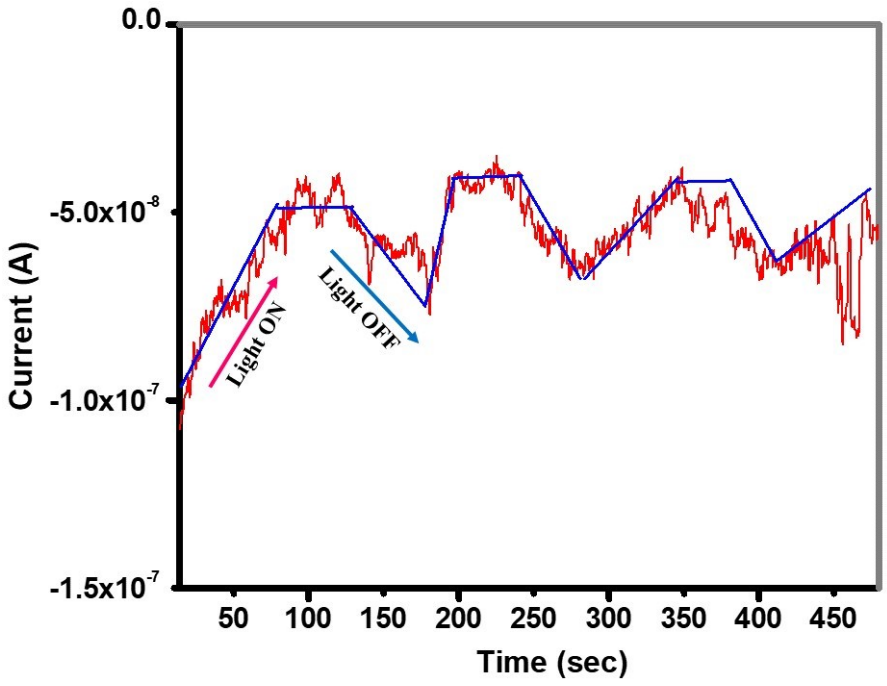

Fig S23. Transient photocurrent responses of **R1**-stainless steel electrode with light ON/OFF cycles under UV- light irradiation (λ_{irr} = 395 nm).

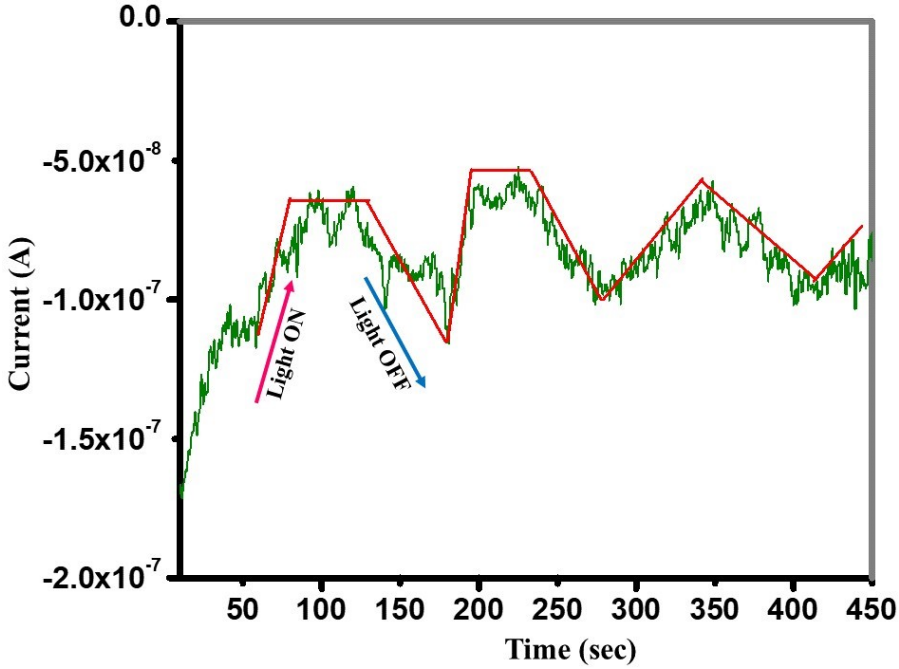

Fig S24. Transient photocurrent responses of **R2-**stainless steel electrode with light ON/OFF cycles under UV- light irradiation (λ_{irr} = 395 nm).

Structural Stability of the complexes

In order to access, the structural stability of the complexes **R1, 1** and **R2**, **the** PXRD pattern of the powder samples of all the complexes was taken before and after HER (**Fig S25-S27**). As can be seen from **Fig S25-S27**, the XRD patterns for all the complexes were found to be similar before and after HER. The peak positions were found to be similar in each of the cases except for the fact that the relative intensities of the peaks were found to be different before and after HER. This accounts for the structural stability of the complexes. Moreover, the PXRD pattern in any of the cases did not show the formation of the Pt XRD pattern. Pt nanoparticles exhibit a particular PXRD pattern in the 2θ range of 40-80°.[25] However, in the case of these three complexes, such kind of PXRD pattern did not appear, which accounted for the fact that the complexes were molecular in nature when used for HER and Pt(II) was the active site for the photocatalytic hydrogen production and not Pt(0)/nanoparticles.

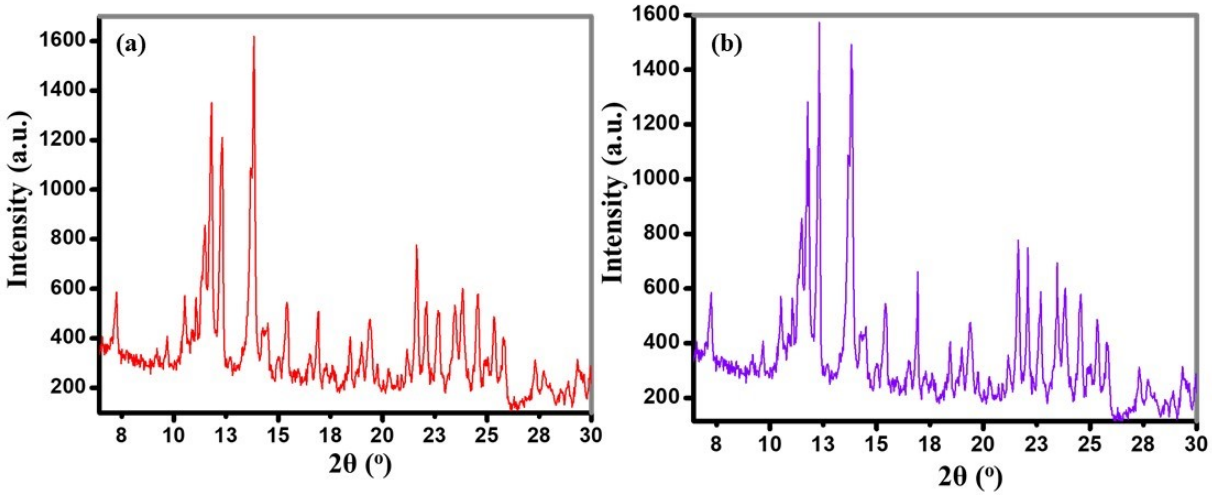

Fig S25. PXRD pattern of **R1** (a) before HER and (b) after HER.

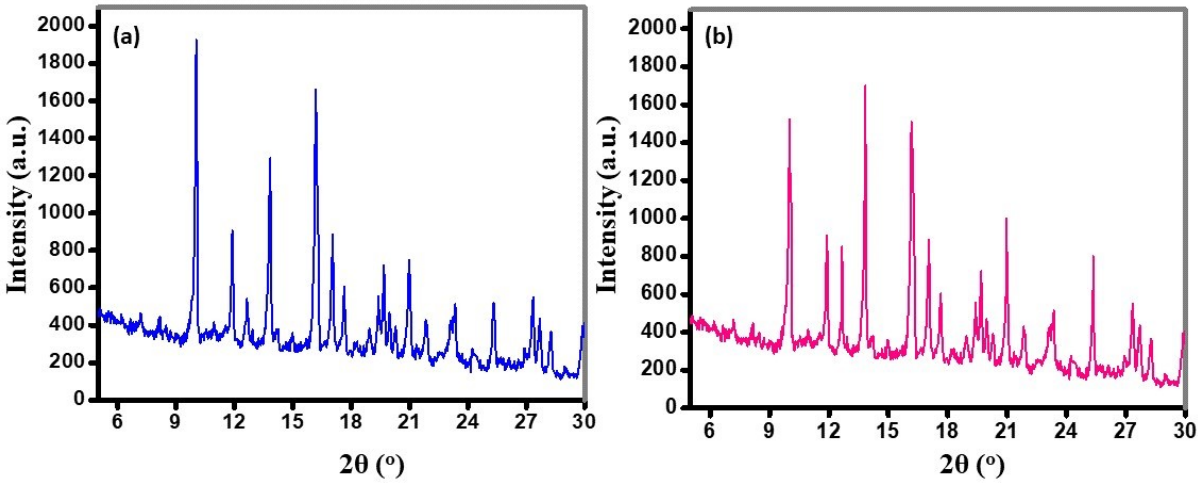

Fig S26. PXRD pattern of **1** (a) before HER and (b) after HER.

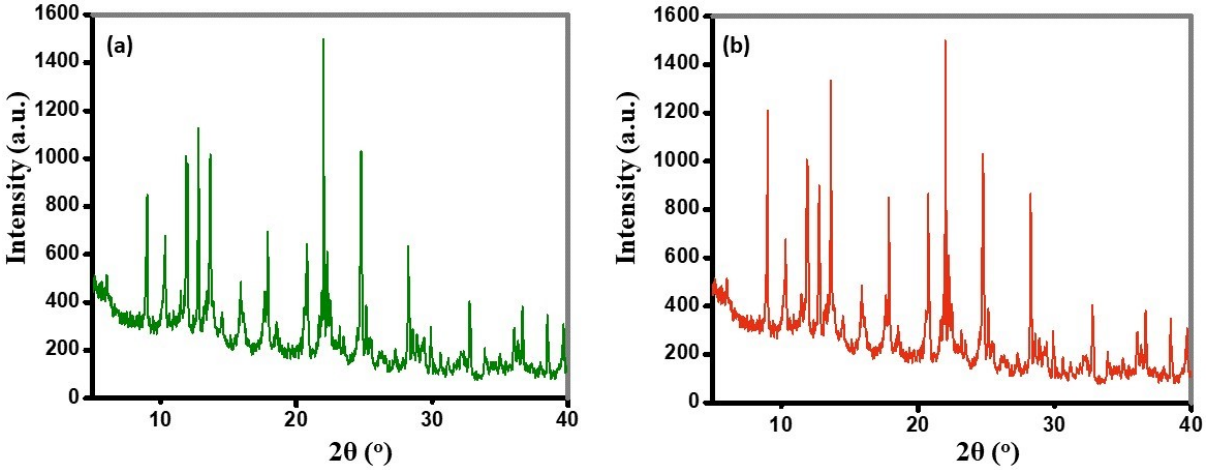

Fig S27. PXRD pattern of **R2** (a) before HER and (b) after HER.

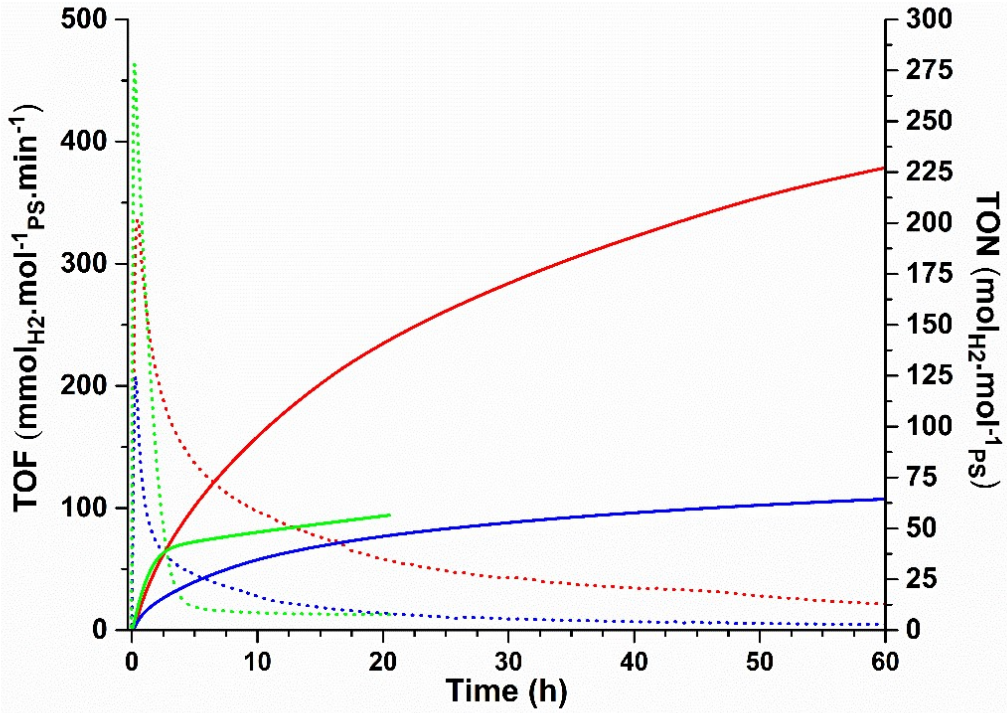

Fig S28. H_2 evolution average of **R1 (red)**, **1 (blue)** and **R2 (green)** alone using 0.5 M TEOA (SED), 0.05 HBF_4 (proton source) and 0.28 M water in DMF. Solid line: TON, dashed line: TOF. Irradiation at 396 nm.

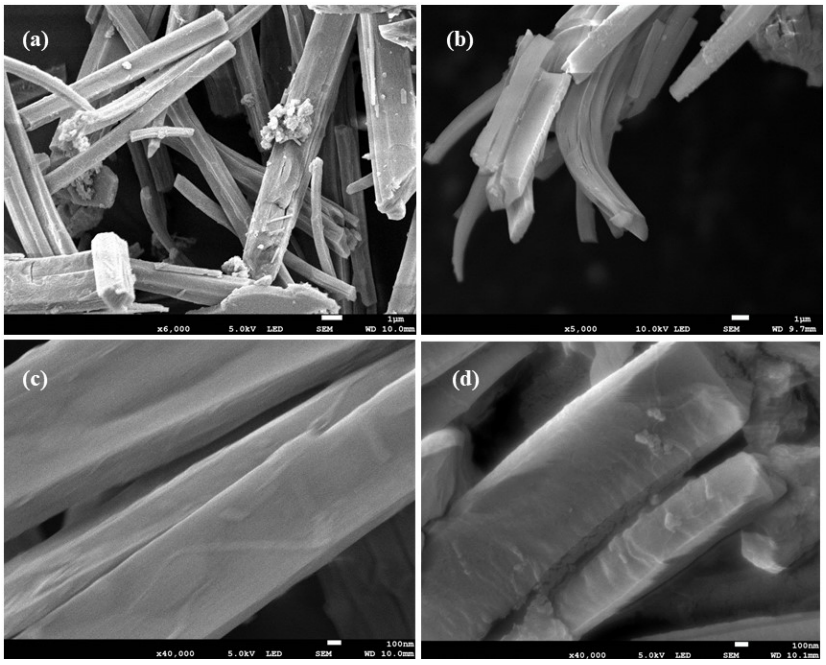

Fig S29. FESEM images of **R1** in DMF (a) before irradiation at a magnification of 1µm and (c) before irradiation at a magnification of 100 nm. (b) after irradiation at a magnification of 1 µm and (d) after irradiation at a magnification of 100 nm.

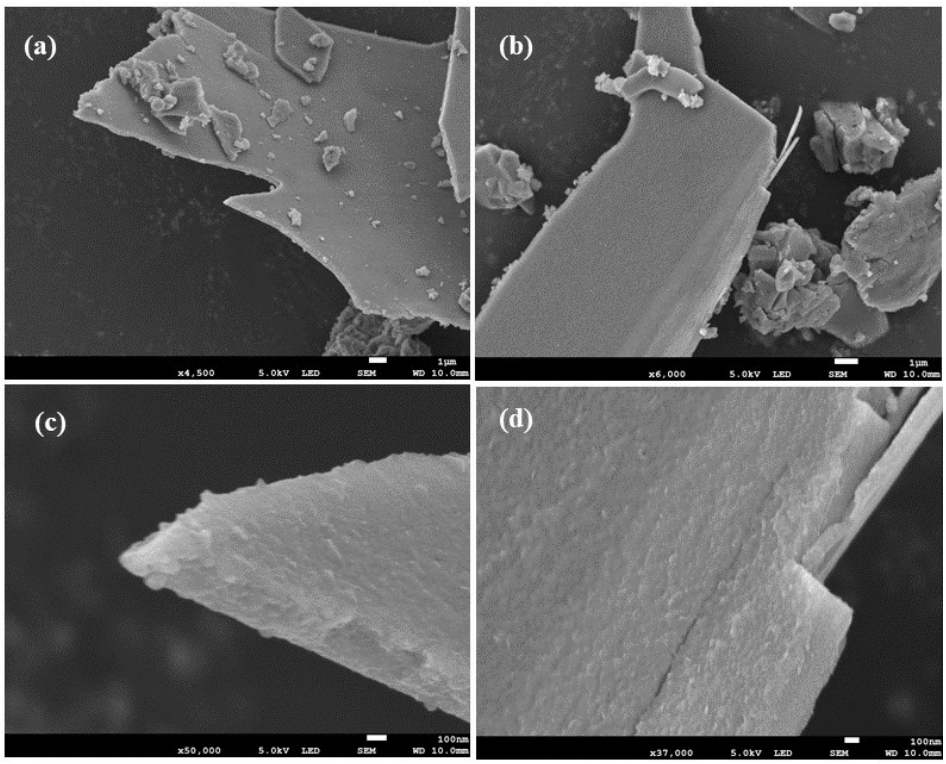

Fig S30. FESEM images of **1** (a) before irradiation at a magnification of 1µm and (c) before irradiation at a magnification of 100 nm. (b) after irradiation at a magnification of 1 µm and (d) after irradiation at a magnification of 100 nm.

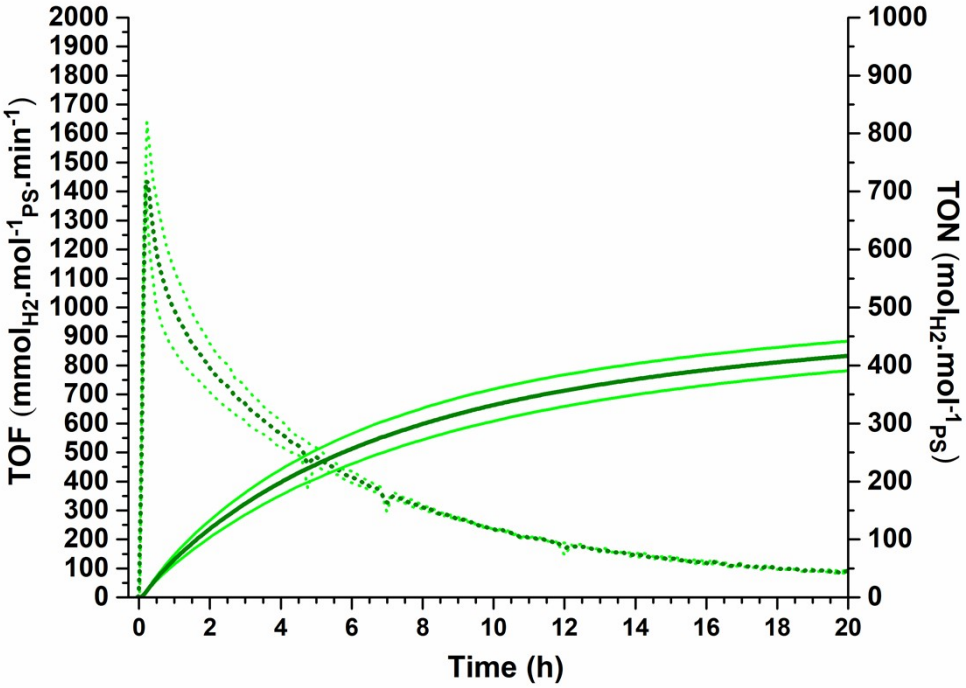

Fig S31. Duplicate of H_2 evolution of the system **R2**/$[Ru(bpy)_3]^{2+}$ (apple green) and the calculated average curve of the duplicate (forest green). Standard deviation of TON for the duplicate is 26 around the average 419. The conditions are 0.5 M TEOA (SED), 0.05 HBF_4 (proton source) and 0.28 M water in DMF. Solid line: TON, dashed line: TOF. Irradiation at 445 nm.

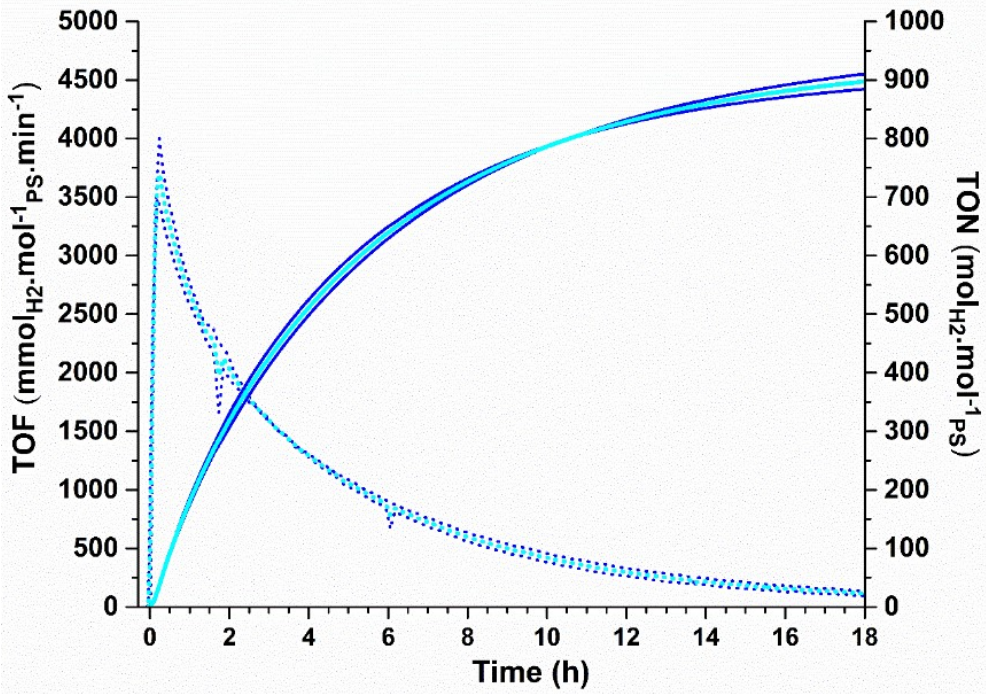

Fig S32. Duplicate of H_2 evolution of the system **1**/$[Ru(bpy)_3]^{2+}$ (deep blue) and the calculated average curve of the duplicate (cyan) Standard deviation of TON for the duplicate is 8 around the average 903. The conditions are 0.5 M TEOA (SED), 0.05 HBF_4 (proton source) and 0.28 M water in DMF. Solid line: TON, dashed line: TOF. Irradiation at 445 nm.

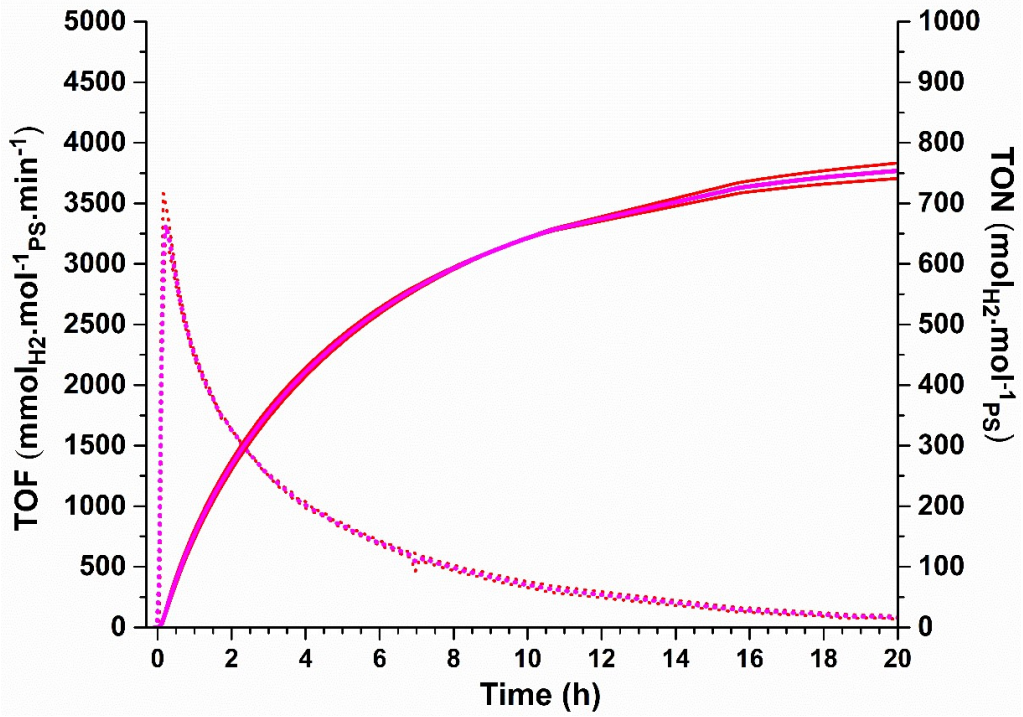

Fig S33. Duplicate of H_2 evolution of the system **R1**/$[Ru(bpy)_3]^{2+}$ (red) and the calculated average curve of the duplicate (majenta) Standard deviation of TON for the duplicate is 16 around the average 774. The conditions are 0.5 M TEOA (SED), 0.05 HBF_4 (proton source) and 0.28 M water in DMF. Solid line: TON, dashed line: TOF. Irradiation at 445 nm.

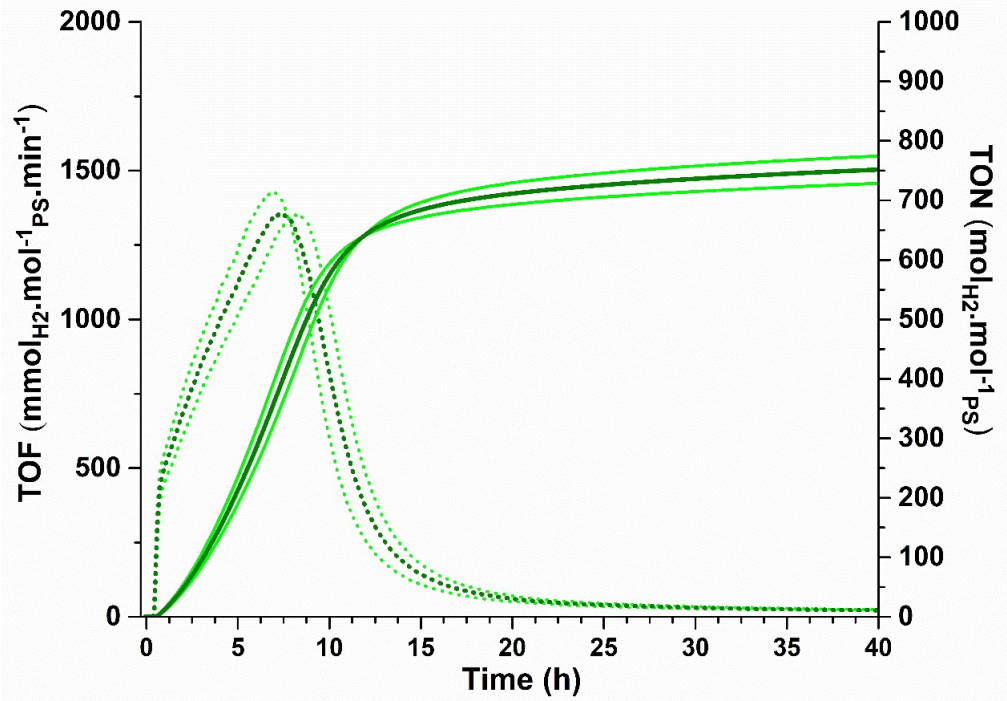

Fig S34. Duplicate of H_2 evolution of the system **R2**/Cobaloxime (apple green) and the calculated average curve of the duplicate (forest green). Standard deviation of TON for the duplicate is 23 around the average 755. The conditions are 0.5 M TEOA (SED), 0.05 HBF_4 (proton source) and 0.28 M water in DMF. Solid line: TON, dashed line: TOF. Irradiation at 396 nm.

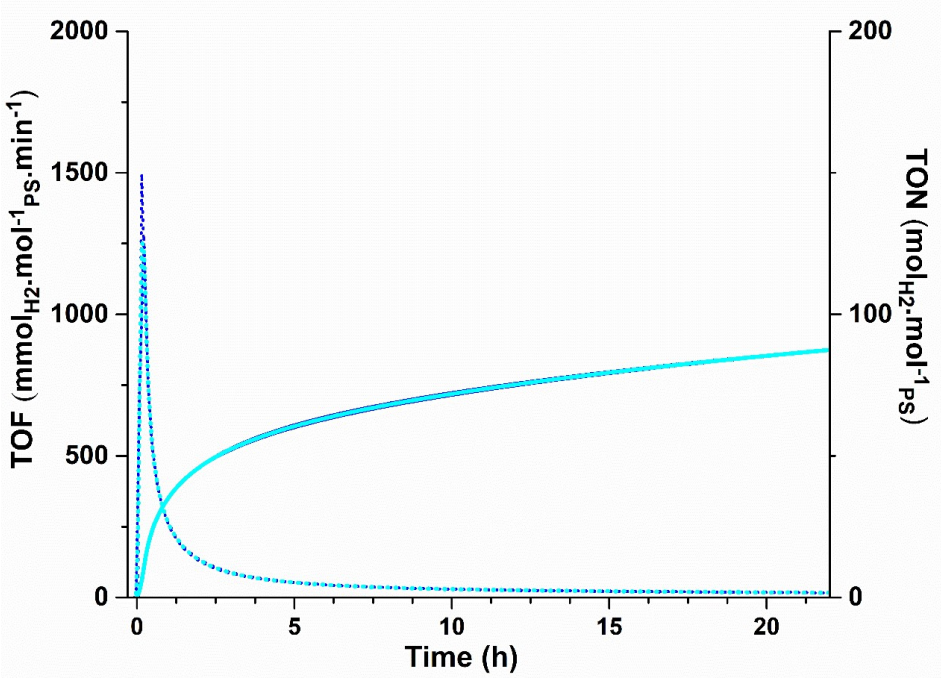

Fig S35. Duplicate of H_2 evolution of the system **1**/Cobaloxime (blue) and the calculated average curve of the duplicate (cyan). Standard deviation of TON for the duplicate is 0,15 around the average 88. The conditions are 0.5 M TEOA (SED), 0.05 HBF_4 (proton source) and 0.28 M water in DMF. Solid line: TON, dashed line: TOF. Irradiation at 396 nm.

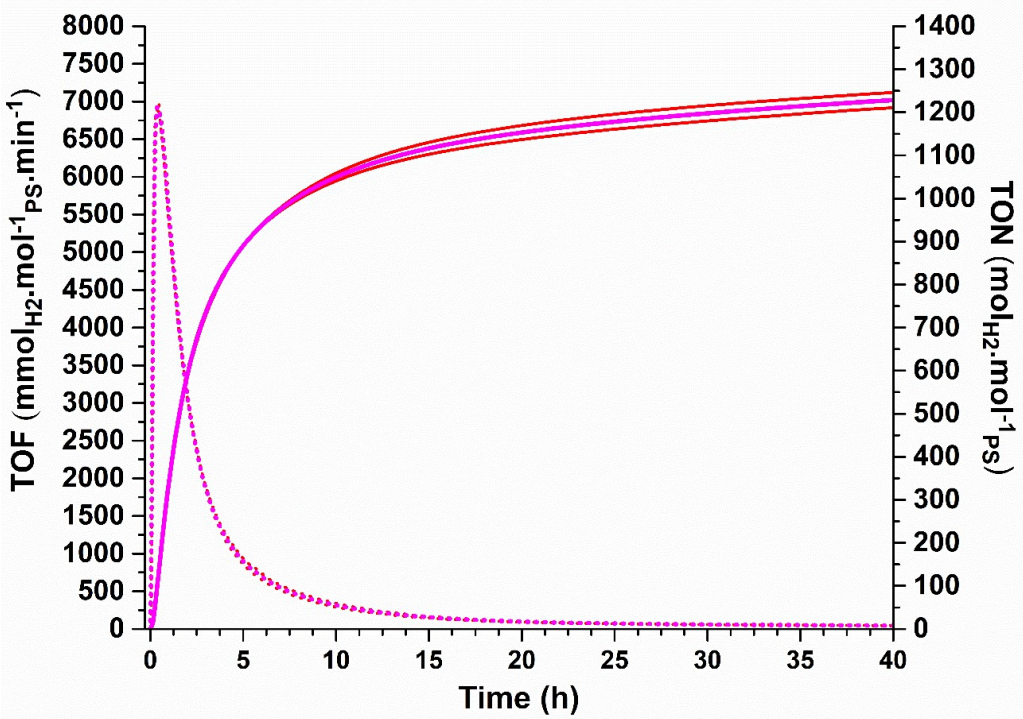

Fig S36. Duplicate of H_2 evolution of the system **R1**/Cobaloxime (red) and the calculated average curve of the duplicate (majenta). Standard deviation of TON for the duplicate is 19 around the average 1229. The conditions are 0.5 M TEOA (SED), 0.05 HBF_4 (proton source) and 0.28 M water in DMF. Solid line: TON, dashed line: TOF. Irradiation at 396 nm.

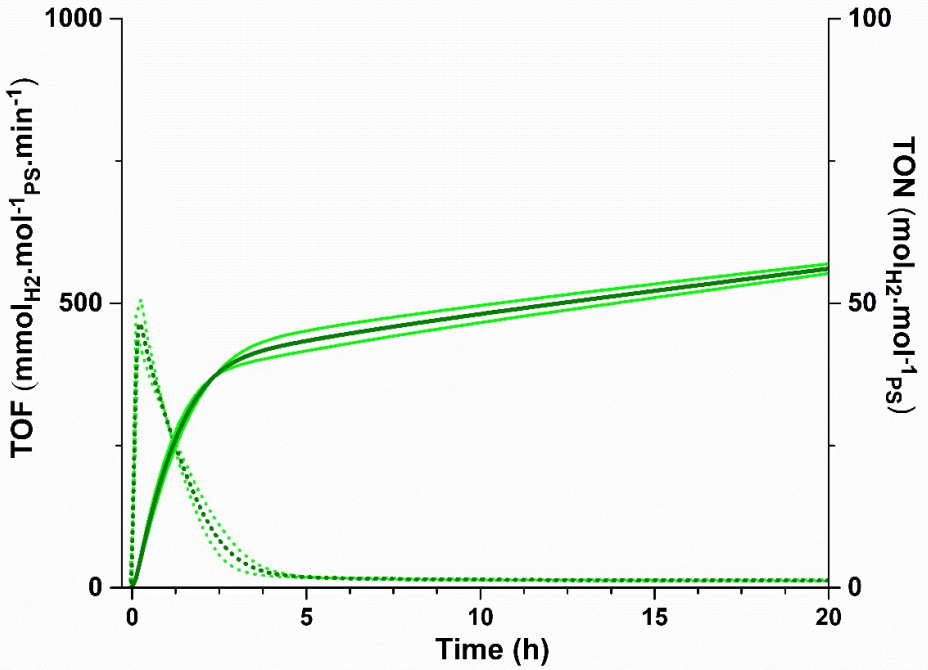

Fig S37. Duplicate of H_2 evolution of **R2** (apple green) and the calculated average curve of the duplicate (forest green). Standard deviation of TON for the duplicate is 1 around the average 56. The conditions are 0.5 M TEOA (SED), 0.05 HBF_4 (proton source) and 0.28 M water in DMF. Solid line: TON, dashed line: TOF. Irradiation at 396 nm.

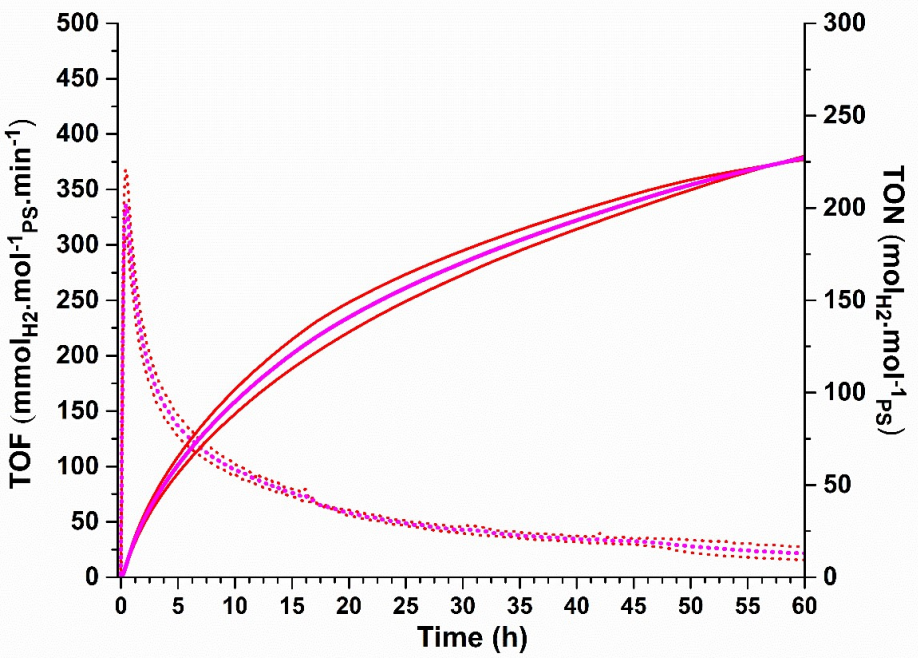

Fig S38. Duplicate of H_2 evolution of the system **R1** (red) and the calculated average curve of the duplicate (majenta). Standard deviation of TON for the duplicate is 1 around the average 227. The conditions are 0.5 M TEOA (SED), 0.05 HBF_4 (proton source) and 0.28 M water in DMF. Solid line: TON, dashed line: TOF. Irradiation at 396 nm.

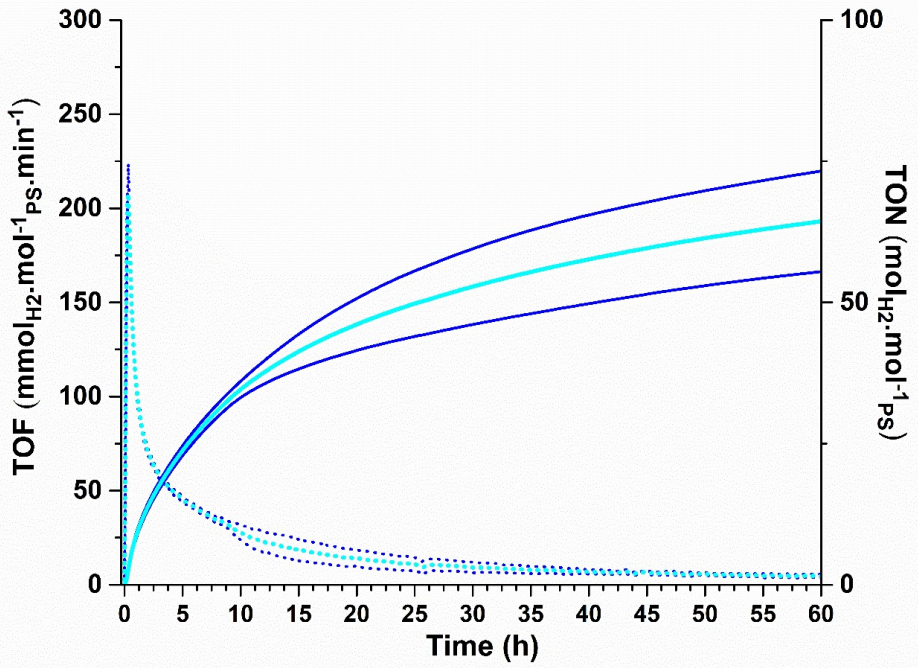

Fig S39. Duplicate of H_2 evolution of the system **1** (blue) and the calculated average curve of the duplicate (cyan). Standard deviation of TON for the duplicate is 9 around the average 65. The conditions are 0.5 M TEOA (SED), 0.05 HBF_4 (proton source) and 0.28 M water in DMF. Solid line: TON, dashed line: TOF. Irradiation at 396 nm.

Table S10. Maxima, width band of emission spectra and photon flux of used LEDs.

	UV	BLUE
λmax(nm)	396	445
Δλ (nm)	70	150
F in $E.s^{-1}$[a]	1.3×10^{-6}	1.3×10^{-6}
P in Watt[a]	0.384	0.346

[a]An analog power-meter PM100A (THORLABS) associated with a compact photodiode power head with silicon detector S120C is used to evaluate the photon flux for each LEDs. Photo-diode detector is placed at the same distance from the LED surface than the bottom of the illuminated vial (3.8 cm^2).

Table S11. Optimized Atomic coordinates obtained from DFT calculations of **[1]**$^+$.

Center Number	Atomic Number	Atomic Type	Coordinates (Angstroms) X	Y	Z
1	6	0	13.688709	2.929669	4.563181
2	6	0	13.449977	1.579813	4.857414
3	7	0	12.195695	1.068681	4.714552
4	6	0	11.169880	1.837756	4.255025
5	6	0	11.409857	3.168284	3.884144
6	6	0	12.669629	3.722242	4.056370
7	6	0	14.579894	0.768675	5.386533
8	6	0	9.797621	1.294843	4.063444
9	6	0	15.871527	1.101309	4.987479
10	6	0	17.018607	0.602058	5.635186
11	6	0	16.881930	-0.187157	6.752518
12	6	0	15.592710	-0.591785	7.182780
13	6	0	14.440604	-0.199164	6.433311
14	6	0	15.404741	-1.386061	8.341971
15	6	0	14.138527	-1.774987	8.707361
16	6	0	13.067961	-1.477559	7.846972
17	7	0	13.218429	-0.752906	6.736729
18	6	0	9.526693	-0.027396	3.583816
19	6	0	8.251864	-0.315220	3.004792
20	6	0	7.205310	0.636787	3.101724
21	6	0	7.426281	1.841834	3.725458
22	6	0	8.722935	2.173965	4.164759
23	7	0	10.471681	-1.024059	3.662393
24	6	0	10.285380	-2.176540	3.016145
25	6	0	9.109504	-2.462018	2.301656
26	6	0	8.074185	-1.559844	2.349685
27	78	0	11.846431	-0.888794	5.198451
28	17	0	11.445834	-3.132233	5.753059
29	1	0	14.666564	3.352451	4.748833

30	1	0	10.611956	3.754291	3.448887
31	1	0	12.854991	4.759819	3.798579
32	1	0	16.007368	1.782152	4.154463
33	1	0	18.001352	0.883197	5.272621
34	1	0	17.750068	-0.520555	7.312731
35	1	0	16.270738	-1.674151	8.930678
36	1	0	13.952592	-2.360614	9.599810
37	1	0	12.080553	-1.881274	8.025499
38	1	0	6.232781	0.390567	2.686731
39	1	0	6.622455	2.560462	3.842516
40	1	0	8.886159	3.160375	4.584682
41	1	0	11.068526	-2.915407	3.118955
42	1	0	9.020159	-3.412158	1.788577
43	1	0	7.116338	-1.781650	1.888333

Table S12. Optimized atomic coordinates obtained from DFT calculations of **[1]**$^{+}$.

Center Number	Atomic Number	Atomic Type	Coordinates (Angstroms) X	Y	Z
1	6	0	13.578837	2.954133	4.687852
2	6	0	13.409506	1.579868	4.940010
3	7	0	12.171496	1.045145	4.774259
4	6	0	11.152597	1.821210	4.320807
5	6	0	11.436402	3.156383	3.977614
6	7	0	12.619369	3.723360	4.185837
7	6	0	14.561943	0.801245	5.446625
8	6	0	9.783338	1.304428	4.099512
9	6	0	15.841620	1.208228	5.075485
10	6	0	17.002222	0.725050	5.709888
11	6	0	16.887336	-0.124342	6.785007
12	6	0	15.612287	-0.598659	7.186510
13	6	0	14.449016	-0.216343	6.449043
14	6	0	15.451326	-1.448674	8.309342
15	6	0	14.198153	-1.893274	8.655622
16	6	0	13.118180	-1.592131	7.809127
17	7	0	13.244049	-0.820032	6.726968
18	6	0	9.505176	-0.013197	3.610148
19	6	0	8.232546	-0.280789	3.016798
20	6	0	7.198783	0.686601	3.102649
21	6	0	7.427980	1.890272	3.726523
22	6	0	8.722153	2.203113	4.184877
23	7	0	10.441104	-1.019265	3.684497
24	6	0	10.245894	-2.162679	3.022991
25	6	0	9.069773	-2.431054	2.303079
26	6	0	8.043528	-1.518709	2.352721
27	78	0	11.843201	-0.919818	5.205183
28	17	0	11.465938	-3.177924	5.700490

29	1	0	14.522735	3.436934	4.915265
30	1	0	10.676034	3.771259	3.509080
31	1	0	15.955240	1.932199	4.276123
32	1	0	17.975787	1.062827	5.372030
33	1	0	17.763984	-0.450892	7.335933
34	1	0	16.325909	-1.731451	8.887776
35	1	0	14.030212	-2.520443	9.523059
36	1	0	12.143055	-2.029206	7.975150
37	1	0	6.228162	0.453986	2.675500
38	1	0	6.633229	2.620782	3.830457
39	1	0	8.894488	3.186080	4.609245
40	1	0	1.023436	-2.908548	3.115440
41	1	0	8.974244	-3.375600	1.780873
42	1	0	7.086433	-1.725771	1.883105

Table S13. Optimized atomic coordinates obtained from DFT calculations of **R2**.

Center Number	Atomic Number	Atomic Type	Coordinates (Angstroms) X	Y	Z
1	6	0	1.176990	3.459763	-0.234354
2	6	0	1.189973	2.052035	-0.269071
3	6	0	0.000151	1.333860	0.000317
4	6	0	-1.189476	2.052476	0.269386
5	6	0	-1.176107	3.460187	0.234060
6	6	0	0.000537	4.160185	-0.000298
7	6	0	2.498068	1.393466	-0.532178
8	6	0	-2.497757	1.394380	0.532748
9	6	0	3.463148	2.047153	-1.293184
10	6	0	4.802241	1.614609	-1.372829
11	6	0	5.218429	0.530162	-0.639268
12	6	0	4.273778	-0.208937	0.116569
13	6	0	2.889737	0.160018	0.086728
14	6	0	4.663156	-1.312405	0.914766
15	6	0	3.716423	-2.011254	1.621443
16	6	0	2.361058	-1.683690	1.440492
17	7	0	1.958568	-0.670419	0.673195
18	6	0	-2.889755	0.160776	-0.085643
19	6	0	-4.273896	-0.207815	-0.115339
20	6	0	-5.218356	0.531865	0.640170
21	6	0	-4.801881	1.616510	1.373275
22	6	0	-3.462668	2.048652	1.293464
23	7	0	-1.958806	-0.670168	-0.671742
24	6	0	-2.361565	-1.683677	-1.438583
25	6	0	-3.717016	-2.010952	-1.619406
26	6	0	-4.663568	-1.311526	-0.913057
27	78	0	-0.000124	-0.656571	0.000734
28	17	0	-0.000489	-3.136764	0.001285

29	1	0	2.100023	4.012928	-0.372005
30	1	0	-2.098988	4.013666	0.371461
31	1	0	3.177800	2.941835	-1.835109
32	1	0	5.505599	2.168226	-1.987320
33	1	0	6.258138	0.216407	-0.631571
34	1	0	5.713980	-1.585515	0.959241
35	1	0	3.976019	-2.846859	2.261153
36	1	0	1.578807	-2.295961	1.867160
37	1	0	-6.258150	0.218389	0.632596
38	1	0	-5.505093	2.170577	1.987526
39	1	0	-3.177083	2.943483	1.835018
40	1	0	-1.579473	-2.296364	-1.864948
41	1	0	-3.976831	-2.846775	-2.258743
42	1	0	-5.714466	-1.584370	-0.957421
43	1	0	0.000686	5.246072	-0.000534

References

1. G. A. Crosby and J. N. Demas, *The Journal of Physical Chemistry*, 1971, **75**, 991-1024.
2. W. H. Melhuish, *The Journal of Physical Chemistry*, 1961, **65**, 229-235.
3. N. C. Greenham, I. D. W. Samuel, G. R. Hayes, R. T. Phillips, Y. A. R. R. Kessener, S. C. Moratti, A. B. Holmes and R. H. Friend, *Chemical Physics Letters*, 1995, **241**, 89-96.
4. N. G. Connelly and W. E. Geiger, *Chemical Reviews*, 1996, **96**, 877-910.
5. M. J. Frisch, G. W. Trucks, H. B. Schlegel, G. E. Scuseria, M. A. Robb, J. R. Cheeseman, G. Scalmani, V. Barone, G. A. Petersson, H. Nakatsuji, X. Li, M. Caricato, A. V. Marenich, J. J. Bloino, B. G., R. Gomperts, B. Mennucci, H. P. Hratchian, J. V. Ortiz, A. F. Izmaylov, J. L. Sonnenberg, D. Williams-Young, F. Ding, F. E. Lipparini, F., J. Goings, B. Peng, A. Petrone, T. Henderson, D. Ranasinghe, V. G. Zakrzewski, J. Gao, N. Rega, G. Zheng, W. Liang, M. Hada, M. Ehara, K. Toyota, R. Fukuda, J. Hasegawa, M. Ishida, T. Nakajima, Y. Honda, O. Kitao, H. Nakai, T. Vreven, K. Throssell, J. A. J. Montgomery, J. E. Peralta, F. Ogliaro, M. J. Bearpark, J. J. Heyd, E. N. Brothers, K. N. Kudin, V. N. Staroverov, T. A. Keith, R. Kobayashi, J. Normand, K. Raghavachari, A. P. Rendell, J. C. Burant, S. S. Iyengar, J. Tomasi, M. Cossi, J. M. Millam, M. Klene, C. Adamo, R. Cammi, J. W. Ochterski, R. L. Martin, K. Morokuma, O. Farkas, J. B. Foresman and D. J. Fox, *Gaussian 16, Revision C.01*, Gaussian, Inc., Wallingford CT, 2019.
6. C. Lee, W. Yang and R. G. Parr, *Physical Review B*, 1988, **37**, 785-789.
7. A. D. M. a. G. S. Chandler, *J. Chem. Phys.* , 1980, **72**, 5639.
8. T. R. Cundari and W. J. Stevens, *: J. Chem. Phys.*, 1993, **98**, 5555 - 5565.
9. M. E. Casida, J. Christine, K. C. Casida and D. R. Salahub, 1998, **108**, 4439 - 4449.
10. R. E. Stratmann, G. E. Scuseriaa and M. J. Frisch, *J. Chem. Phys.* , 1998, **109**.
11. W. R. Browne, N. M. O'Boyle, J. J. McGarvey and J. G. Vos, *Chemical Society Reviews*, 2005, **34**, 641-663.
12. N. M. O'boyle, A. L. Tenderholt and K. M. Langner, *Journal of Computational Chemistry*, 2008, **29**, 839-845.
13. G G. A. Zhurko and D. A. Zhurko, ChemCraft 1.5, Plimus, San Diago, CA. Available at: https://www.chemcraftprog.com/.

14. L. Skripnikov, Chemissian v4.42, 2005–2016, Available at: https://www.chemissian.com/.
15. M. Jäger, L. Eriksson, J. Bergquist and O. Johansson, *The Journal of Organic Chemistry*, 2007, **72**, 10227-10230.
16. S. Sharma, B. Sharma and A. K. Pal, *Journal of Photochemistry and Photobiology A: Chemistry*, 2023, **442**, 114778.
17. K. L. Garner, L. F. Parkes, J. D. Piper and J. A. G. Williams, *Inorganic Chemistry*, 2010, **49**, 476-487.
18. R. J. Ortiz, J. D. Braun, J. A. G. Williams and D. E. Herbert, *Inorganic Chemistry*, 2021, **60**, 16881-16894.
19. J. W. Palmer, W. E. Swartz, D. King and J. A. Stanko, *Florida Scientist*, 1993, **56**, 123-128.
20. C. D. Wagner, *Faraday Discussions of the Chemical Society*, 1975, **60**, 291-300.
21. D. Shuzhong, X. Fanhua and D. Jingfa, *Journal of Catalysis*, 1988, **109**, 170-179.
22. J. R. Araujo, B. S. Archanjo, K. R. de Souza, W. Kwapinski, N. P. S. Falcão, E. H. Novotny and C. A. Achete, *Biology and Fertility of Soils*, 2014, **50**, 1223-1232.
23. N. Sinha, B. Pfund, C. Wegeberg, A. Prescimone and O. S. Wenger, *Journal of the American Chemical Society*, 2022, **144**, 9859-9873.
24. X. Bai, L. Wang and Y. Zhu, *ACS Catalysis*, 2012, **2**, 2769-2778.
25. J. Zhang, L. Lin and H. Cui, *Nanomaterials (Basel)*, 2020, **10**.